PS 197

CERN/PSCC/85-56
PSCC/P90
11 October, 1985

PROPOSAL

THE CRYSTAL BARREL: MESON SPECTROSCOPY AT LEAR WITH A 4π NEUTRAL AND CHARGED DETECTOR

E. Aker[1], C. Amsler[2], T. Armstrong[3], P. Birien[4], J. Bistirlich[5], D.V. Bugg[6*], G. Bueche[1], S. Cierjacks[1], A.S. Clough[7], K.M. Crowe[5], D. Engelhardt[1], M.Gee[8], M. Guckes[9], A. Hahn[8], G. Hall[6], A. Hasan[3], T. Henkes[1], H. Kalinowsky[9], E. Klempt[9], H. Koch[1], A. Kreissl[1*], M. Kunze[1], R. Lewis[3], M. Mandelkern[8], C.A. Meyer[5], S. Playfer[3], R. Rieger[9], D. Rohmann[1], W. Rohrbach[1], B. Schmid[2], W. Schott[1], J. Schultz[8], R.L. Shypit[7], G.A. Smith[3], U. Straumann[9], M. Suffert[10], P.Truöl[2], H. Vonach[11], D. Walther[1], W. Weidenauer[9], J. Whitmore[3], W. Wodrich[12] and C. Zupancic[12].

CRYSTAL BARREL COLLABORATION

[1] Kernforschungszentrum (KfK) & Universität Karlsruhe, FRG.
[2] Universität Zürich, Switzerland.
[3] Pennsylvania State University, University Park, Pennsylvania, USA.
[4] CERN visitor, Geneva, Switzerland.
[5] Lawrence Berkeley Laboratory, University of California, Berkeley, USA.
[6] Queen Mary College, London, UK.
[7] University of Surrey, Guildford, UK.
[8] University of California, Irvine, USA.
[9] Universität Mainz, FRG.
[10] Centre de Recherches Nucléaires, Strasbourg, France.
[11] Institut für Radiumforschung & Universität, Wien, Austria.
[12] Universität München, FRG.

[*] presently at CERN, Geneva, Switzerland

Spokesman: H. Koch Contactman: C. Amsler

CERN LIBRARIES, GENEVA

CM-P00059061

CONTENTS

1. SUMMARY

The physics goals of greatest relevance and highest priority in the Crystal Barrel experiment concern QCD related problems. The basic lines of research involve meson spectroscopy, analyses bearing on the quark and/or gluon content of states, and exploration of mechanisms and rules which govern $\bar{p}p$ annihilation dynamics. Special emphasis will be put on the investigation of annihilation channels of the all neutral category or with several neutrals (π^0 or η) in the final state for which little or no data exist. The main goals can be summarized as follows:

1. Search for glueballs and hybrids. Although most of the charged and neutral channels will be accessible in this experiment, we favour especially decay channels like $\pi^0\pi^0$, $\eta\eta$, $\pi^0\eta$, $\pi^0\pi^0\eta$, $\pi^+\pi^-\eta$ and $K\bar{K}\pi$, as well as those involving the η'.

2. Study of radiative and rare meson decays for which the excellent photon detection capability of the apparatus is well suited.

3. Study of the $\bar{p}p$ annihilation dynamics. In particular we will measure the branching ratios for annihilation at rest into two or three mesons from atomic S or P states. Favourite neutral channels are $\pi^0\pi^0$, $\pi^0\gamma$, $\pi^0\eta(\eta')$, $\pi^0\omega$ and $\eta\eta(\eta')$.

4. Search for $\bar{p}p$ bound states at rest where we can look for monochromatic γ and π^0 transitions in exclusive final states.

5. There are strong motivations for scanning momenta in reasonably small steps. These include the possibility of looking for anomalies or enhancements in cross sections for exclusive final states, as well as the desire to map the cross sections as functions of energy for all possible two body final states which can then be subject to phase – shift analyses.

The proposed Crystal Barrel Detector will be a comprehensive and powerful instrument. It will detect and identify charged and neutral particles over essentially 4π solid angle with a detection efficiency close to 100 %. Although nearly all annihilation channels, even complicated ones, will be accessible to the experiment, the combinatorial background to reconstruct intermediate resonances is often reduced in final states with more than one neutral.

Annihilation at rest with initial angular momentum $L(\bar{p}p) = 0$ will be studied with a liquid hydrogen target. Annihilation at rest with $L = 1$ will be investigated with a gaseous hydrogen target and a trigger on atomic L X – rays. A fast online selection of specific annihilation channels will be carried out.

We propose to begin running with a stopping beam of 200 MeV/c. This facilitates an early study of the apparatus and the properties and resolution of the detector. Moving to higher momentum with a liquid target serves principally the purpose of studying higher mass states. Thus we could study properties of higher mass glueball candidates produced in exclusive final states. For this purpose it is best to take a large run at the highest beam momentum available from LEAR, nominally 2 GeV/c, which allows coverage of the range containing most current glueball candidates.

The detector, and in particular the Crystal Barrel itself, is designed so that it could be operated later in the colliding mode of LEAR.

2. PHYSICS MOTIVATIONS

2.1 Introduction

The central issue of the proposed experiment is the search for boson resonances with constituent gluons: for glueballs, bound states of two or more gluons forming a colour singlet, and for hybrids (also called hermaphrodites or meiktons) in which the colour 8 of a $3 \times \bar{3}$ quark−antiquark pair is neutralized by a constituent gluon.

Glueballs and hybrids are striking predictions of quantum chromodynamics, the presently accepted theory of strong interactions which has made remarkably successful predictions for large p_T processes. However for low energy phenomena the theory is far from being fully tested or understood. The experimental verification of the existence of hadronic states with constituent gluons would therefore be an important milestone in our understanding of low−energy QCD; a mass spectrum of glueballs and hybrids and knowledge of their preferred decay modes would be a guideline for further theoretical and experimental research.

Even though several glueball candidates exist (one of the most convincing ones, the $\iota(1440)$, was originally discovered in $\bar{p}p$ annihilations at rest and named the E meson), there is so far no completely conclusive evidence for their glueball interpretation. The situation is even worse in the case of hybrids where at present not even a strong candidate exists.

Glueballs have been sought in processes where hard gluons are expected to dominate the intermediate state, like radiative Ψ decay, $\phi\phi$ production or double Pomeron exchange. On the other hand, spherical glueball bags are unstable and glueballs may rather exist as flux tubes of toroidal shape. The most appropriate production mechanism is therefore difficult to judge and an extended quark−gluon object like $\bar{p}p$ annihilation might be a good glueball source. In any case we expect $\bar{p}p$ annihilation to be well suited to produce hybrid states.

The reputable $q\bar{q}$ mesons and meson candidates are shown in Fig. 1, with a conventional assignment to SU(3) nonets. Since we orient this proposal towards providing information on glueballs and hybrids, we shall discuss conventional $q\bar{q}$ spectroscopy only to the extent that it is intertwined with the spectroscopy of novel states.

2.2 Glueballs

Glueballs are I = 0, SU(3) singlet bound states of two (or more) gluons. These and exotic states $q\bar{q}g$ and $qqq\bar{q}$ are predicted in the mass range 600 MeV upwards. Prominent candidates are the $J^{PC} = 0^{-+}$ $\iota(1440)$, 0^{++} G(1590), 2^{++} $\theta(1690)$, 2^{++}(?) $\xi(2220)$ and 2^{++} $g_T(2120,2220,2360)$. However, positive identification has proved elusive, because of possible confusion with $q\bar{q}$ orbital and radial excitations. For recent reviews see for example ref [1].

Lattice QCD calculations firmly predict the existence of glueballs. The mass scale parameter can be determined from the ρ mass or from the string tension, giving a ground state, $J^{PC} = 0^{++}$ at 660 MeV and a series of further states up to 3.5 GeV [2]. The most obvious candidates for the low mass glueballs are the $\epsilon(700)$, the $\iota(1440)$ and the $\theta(1690)$. Apart from lattice QCD, QCD sum rules[3], potential models[4], flux tube models[5] and bag models[6] agree that glueball should exist.

The simplest model is the MIT bag model of Jaffe and Johnson[6]. For a discussion of J^{PC} assignment, we follow this as a framework. In a spherical bag, a transverse electric (TE) gluon has $J^{PC} = 1^{+-}$, S = 1 and L = 1; a transverse magnetic (TM) gluon has $J^{PC} = 1^{--}$, S = 1 and L a linear combination of 0 and 2. For bag radius R, TE gluons have lower mass (2.74/R) than TM gluons (4.49/R). Jaffe and Johnson predicted that $(TE)^2$ glueballs would be lowest around 960 MeV with $J^{PC} = 0^{++}$ and 2^{++}; (TE)(TM) would come next with $J^{PC} = 0^{-+}$ and 2^{-+}, followed by $(TM)^2$, 0^{++} and 2^{++} around 1600 MeV. However, multi−gluon interactions can shift relative TE and TM masses and can introduce spin splittings of hundreds of MeV, so the mass scale is very uncertain. Predictions of the MIT bag model are shown in Table 1.

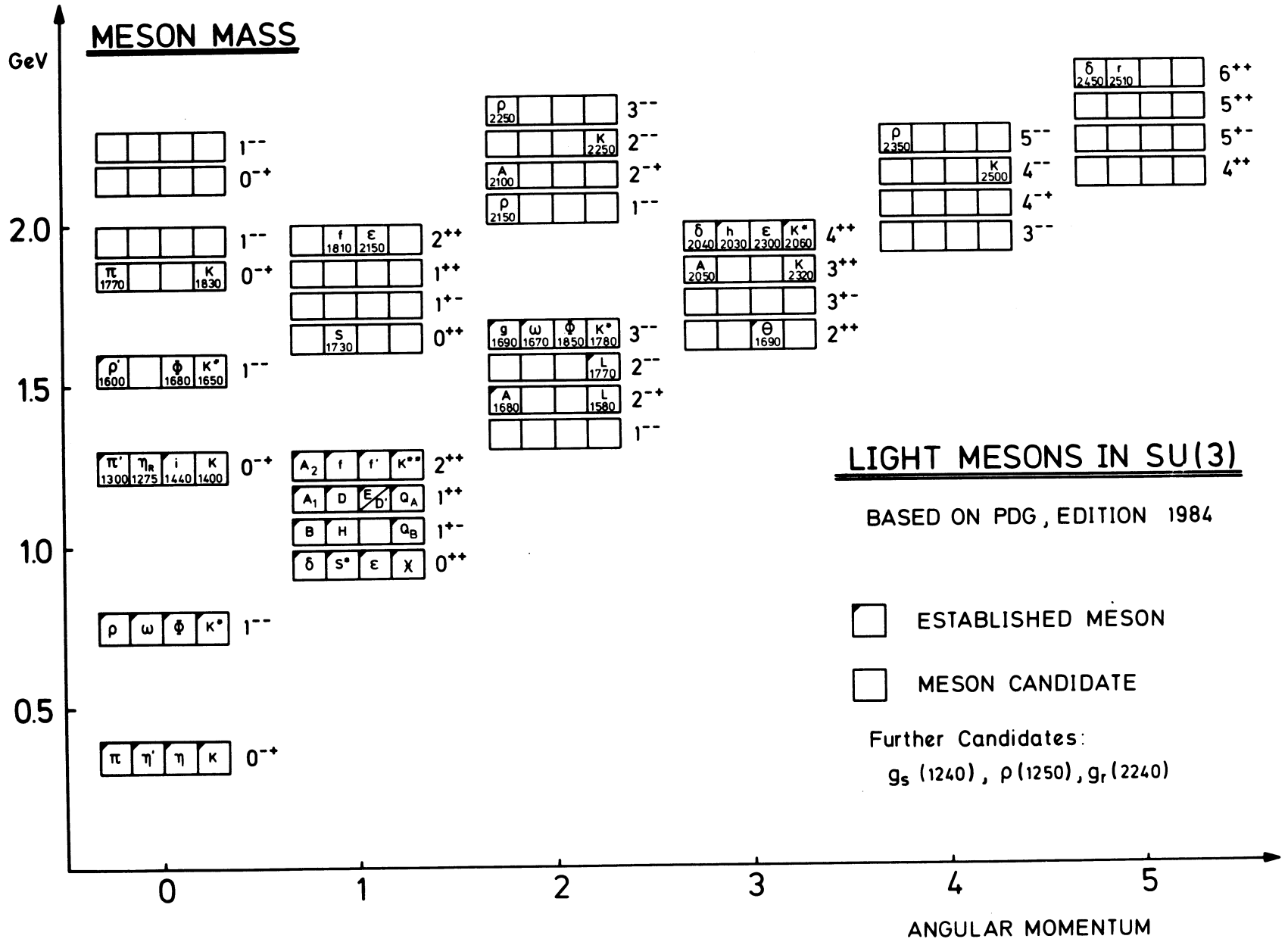

Fig. 1: Status of $q\bar{q}$ nonets.
The mass scale is determined by the $u\bar{u}$ ($d\bar{d}$) mesons.

J^{PC}		Mass [MeV]
$0^{++},2^{++}$	$(TE)^2$	960
$0^{-+},1^{-+},2^{-+}$	(TE)(TM)	1290
$0^{+-},1^{++},2^{+-},3^{++}$	$(TE)^3$	1460
$0^{++},2^{++}$	$(TM)^2$	1590

Table 1: Glueball masses from the MIT bag model[6].

There is mounting evidence[7,8] that the $\theta(1690)$ having $J^{PC}=2^{++}$ is a $(TM)^2$ glueball. This hypothesis is capable of describing its branching ratio into $\pi\pi$, $\eta\eta$ and $\bar{K}K$, and also its helicity amplitudes in $\Psi/J \to \gamma\theta$; conversely, $q\bar{q}$ assignments have trouble with both, and the ground state 2^{++} nonet is so well known that an extra state does not fit in readily. The $\iota(1440)$, $J^{PC}=0^{-+}$ has long been a candidate for a (TE)(TM) glueball[9], but with some $q\bar{q}$ admixture; it is easily confused with the first 0^{-+} radial excitation, whose members are poorly established.

If one tentatively adopts these identifications, there should be a 0^{++} $(TM)^2$ state close to the θ; the G(1590) is a candidate. There is also likely to be a 2^{-+} (TE)(TM) state in the range $1400-1700$ MeV. For this, there is no candidate; it is unlikely to be produced strongly in Ψ/J radiative decays[10,11]. The $(TE)^2$ glueballs 0^{++} and 2^{++} are likewise missing. The former could be one of the states presently ascribed to the $q\bar{q}$ nonet; most are poorly established. Rosner[12] has suggested that the f and f' may mix with gg; there are several candidates [13-15] for an additional 2^{++} $I=0$ state around 1440 MeV. Distinctive features which may help in identifying glueballs are as follows:

1. They are SU(3) singlets. Hence, in the absence of phase space factors and dynamical effects, one expects

$$\Gamma(\pi\pi) = (3/4)\Gamma(K\bar{K}) = 3\Gamma(\eta\eta).$$

However, Chanowitz and Sharpe[16] argue that TM gluons are likely to couple dynamically to $s\bar{s}$ more strongly than $u\bar{u}$ and $d\bar{d}$. Also, η coupling to gluons is enhanced by the triangle anomaly[17,18]. Thus, until experiment establishes a pattern, flavour coupling is a perilous basis for identifying glueballs. Strong coupling to η or K is a signature.

2. Coupling to photons is distinctive, because the electromagnetic operator is well known and can be treated perturbatively, and, in a negative sense, because the gluon does not couple directly to photons.

3. Helicity amplitudes are sensitive to the L content of states. In particular $(TM)^2$ glueballs contain components up to $L=4$, $S=2$ and (TE)(TM) up to $L=3$, $S=2$ in a mass range where a $q\bar{q}$ state is likely to be restricted to $L=2$. These large L components may show up (providing there is enough phase space) in the production mechanism or the decay (e.g. via L.S. or tensor coupling to mesons, such as the ω, with $S\geq 1$).

4. The two-body final states shown in Table 2 couple to $q\bar{q}$ and exotic (non $q\bar{q}$) states. A spin-parity analysis of a structure observed to decay into one of these channels could lead to to the unambiguous identification of an exotic state.

J^{PC}	Decay channels
0^{--}	$\omega\pi$, $\phi\pi$, $\phi\eta$, $\omega\eta$
1^{-+}	$\pi\eta$, $f\pi$, $f'\pi$, $\phi\phi$, $\eta\eta'$
2^{+-}	$\omega\pi$, $\eta\phi$
3^{-+}	$\pi\eta$, $f\pi$, $f'\pi$, $\phi\phi$, $\eta\eta'$

Table 2: Channels coupling to exotic quantum numbers.

Detailed discussions of studies proposed here will be deferred until the section on $q\bar{q}$ nonets. However, in general terms, this experiment can contribute distinctively via its good γ, η and K detection. Good channels to search are $\eta\eta$, $\eta\pi\pi$, $\eta\eta'$, $\bar{K}K$ and $K^*\bar{K}$. For example, the missing 2^{-+} glueball might appear as $\eta\pi\pi$.

2.3 Hybrids

Unlike glueballs, hybrids appear also as $I=1/2$ and $I=1$ states. The lowest states are made from quarks and gluons in a relative S wave. If the $q\bar{q}$ has 0^{-+}, a TE gluon will result with $J^{PC}=1^{--}$. For $q\bar{q}=1^{--}$, three states 0^{-+},1^{-+} and 2^{-+} are possible. The exotic 1^{-+} combination is particularly interesting, since it cannot be confused with a $q\bar{q}$ state. States made from TM gluons have the opposite parity.

Specific advice on decay modes is available from Isgur and Paton [5], who proposed a model where two quarks are connected by a flux-tube (or string) made of a superposition of many gluons. In this model, classic $q\bar{q}$ states are those rotating like dumbbells about the normal to the string. Radial $q\bar{q}$ excitations are vibrations along the string. Exotic states are those where the string itself is excited, either rotating about the axis of the system like a skipping rope or vibrating like a stretched elastic band. Isgur, Kokoski and Paton [19] show that such exotic states decay preferentially to final states with one meson excited (e.g. $B(1235)\pi$, $D(1285)\pi$, $K^*(1420)K$) and this may be why they have so far escaped detection. Table 3 gives their predictions for J^{PG}, decay modes and partial widths. In $\bar{p}p \to \pi X$, the quark rearrangement is sufficiently violent that there seems a good chance of exciting such exotic states.

We propose to search for $\bar{p}p \to \pi^{\pm}X^{\mp}$ or π^0X^0 with X decaying to $D\pi$ or $B\pi$. In $\bar{p}p \to \pi^+\pi^-B^0$ ($B^0 \to \omega\pi^0$, $\omega \to \pi^0\gamma$) and $\bar{p}p \to \pi^{\pm}\pi^0B^{\mp}$ ($B^{\mp} \to \omega\pi^{\mp}$, $\omega \to \pi^0\gamma$), the combinatorial background will be minimized by choosing the $\omega \to \pi^0\gamma$ decay. In $\bar{p}p \to \pi^{\pm}X^{\mp}$ ($X^{\mp} \to D\pi^{\mp}$, $D \to \eta\pi^0\pi^0$) and $\bar{p}p \to \pi^0X^0$ ($X^0 \to D\pi^0$, $D \to \eta\pi^+\pi^-$), a δ cut on the four $\eta\pi^{\pm,0}$ combinations will again reduce combinatorial background. If the 1^{-+} hybrid exists with a low mass, its only decay mode would be $\eta\pi$. Hence we will study $\bar{p}p \to \pi^+\pi^-\eta$ ($\eta \to \gamma\gamma$).

Hybrid state[a]	J^{PG}	(Decay mode)$_{L \text{ of decay}}$	Partial width (MeV)
$x_2^{+-}(1900)$	2^{++}	$(\pi A_2)_P$	450
		$(\pi A_1)_P$	100
		$(\pi H)_P$	150
$y_2^{+-}(1900)$	2^{+-}	$(\pi B)_P$	500
$z_2^{+-}(2100)$	2^{+-}	$[\bar{K}K^*(1420)+\text{c.c.}]_P$	250
		$(\bar{K}Q_2+\text{c.c.})_P$	200
$x_1^{-+}(1900)$	1^{--}	$(\pi B)_{S,D}$	100,30
		$(\pi D)_{S,D}$	30,20
$y_1^{-+}(1900)$	1^{-+}	$(\pi A_1)_{S,D}$	100,70
		$[\pi\pi(1300)]_P$	100
		$(\bar{K}Q_2+\text{c.c.})_S$	~ 100
$z_1^{-+}(2100)$		$(\bar{K}Q_1+\text{c.c.})_D$	80
		$(\bar{K}Q_2+\text{c.c.})_S$	250
		$[\bar{K}K(1400)+\text{c.c.}]_P$	30
$x_0^{+-}(1900)$	0^{++}	$(\pi A_1)_P$	800
		$(\pi H)_P$	100
		$[\pi\pi(1300)]_S$	900
$y_0^{+-}(1900)$	0^{+-}	$(\pi B)_P$	250
$z_0^{+-}(2100)$	0^{+-}	$(\bar{K}Q_1+\text{c.c.})_P$	800
		$(\bar{K}Q_2+\text{c.c.})_P$	50
		$[\bar{K}K(1400)+\text{c.c.}]_S$	800

[a] x, y, and z denote the flavor states $(1/\sqrt{2})(u\bar{u}-d\bar{d})$, $(1/\sqrt{2})(u\bar{u}+d\bar{d})$, and $s\bar{s}$. The subscript on a state is J; the superscripts are P and C_n.

Table 3: Low lying hybrid mesons (from ref [19])

2.4 *Review of $q\bar{q}$ Nonets*

A recent review can be found in ref [21]. In the following we review briefly the normal mesons against which glueballs or hybrids will have to be discriminated. We discuss in particular final states which can be well identified in the Crystal Barrel detector and which are expected to have a low background.

We select specific final states which have least combinatorial background. For example, in the reaction $\bar{p}p \to \pi^{\pm}B^{\mp}$ ($B^{\mp} \to \omega\pi^{\mp}$, $\omega \to \pi^+\pi^-\pi^0$) there are four entries per event to form an ω and then two entries to form a $B^{\pm}$. In this experiment we would choose $\bar{p}p \to \pi^{\pm}B^{\mp}$ ($B^{\mp} \to \omega\pi^{\mp}$, $\omega \to \pi^0\gamma$) for which there are 3 combinations of γ pairs. Only one combination forms a π^0, since the background from the wrong combinations is negligible due to the good π^0 mass resolution. Therefore there will be only two entries per event in the $\omega\pi^{\pm}$ mass plot instead of eight. In the following we will always select the best suited final states.

Table 4 shows which channels can couple to particular quantum numbers.

J^{PC}	I^G	$\pi^0\rho^0$	$\rho^0\rho^0$	$\rho^0\eta$	$\rho^0\omega$	$\rho^0 f$	ωf	$\pi^0 f$	$\pi^0\pi^0$	$\pi^0\omega$	$\pi^0\eta$	$\eta\eta$	$\eta\omega$
0^{-+}	0^+		x										
0^{++}	0^+		x						x			x	
0^{-+}	1^-				x			x					
0^{++}	1^-				x						x		
1^{+-}	0^-	x					x						x
1^{++}	0^+		x										
1^{--}	0^-	x					x						x
1^{+-}	1^+			x		x				x			
1^{++}	1^-				x			x					
1^{--}	1^+			x		x				x			
2^{-+}	0^+		x										
2^{--}	0^-	x					x						x
2^{++}	0^+		x						x			x	
2^{-+}	1^-				x			x					
2^{--}	1^+			x		x				x			
2^{++}	1^-				x			x			x		

Table 4: Quantum numbers (x) of two−meson states (from ref [20]).

2.4.1 0^{-+}:

High mass 0^{-+} mesons can only be radial excitations or exotic states. The existing candidates [$\pi'(1300)$, $\eta_R(1275)$, ι/E(1440), K'(1400)] do not form a reasonable nonet, so at least one must be misidentified or be an exotic state. Table 5 summarises the present knowledge on the two isoscalar states. Note that the E was discovered in $\bar{p}p$ annihilation at rest in its $KK\pi$ decay mode with a branching ratio of 2×10^{-3} [22]. Both η_R and E decay into $\eta\pi\pi$ via an intermediate δ while the ι is seen only to decay via $\delta\pi$ into $\bar{K}K\pi$. Obviously further experimental clarification is needed. The radial excitation of the η', expected around 1600 MeV, is still missing.

In radiative J/Ψ decay, the $\eta\pi\pi$ final state is observed to resonate in the mass range 1.6 – 1.9 GeV.

Mass	Width	J^{PC}	Decay	Reference
E/ι				
1425	80	0^{-+}	$K_SK\pi$	P. Baillon et al., Nuov. Cim. 50A(1967)393.
1398	50		$\eta\pi^+\pi^-$	C. Defoix et al.,Nucl. Phys. B44(1972)125.
1426	40	1^{++}	$K_SK\pi$	C. Dionisi et al.,Nucl. Phys. B169(1980)1.
1420			$\eta\pi^0\pi^0$	J.P. Stroot, CERN EP 85 – 01,1985.
1420	60	0^{-+}	$K_SK\pi$	S.U. Chung et al.,PRL 55(1985)779.
1425	62	1^{++}	$K\bar{K}\pi$	T.A. Armstrong et al.,PL 146B(1984)273.
1456	95	0^{-+}	$K\bar{K}\pi$	J.D.Richman,Thesis,CALT – 68 – 1231,1985.
1440	55	0^{-+}	$K^+K^-\pi$	C. Edwards et al.,PRL 49(1982)259.
1422	47		$K\bar{K}\pi$	P.Chauvat et al.,CERN EP 84 – 122.
1420		0^{-+}	$\eta\pi^+\pi^-$	A. Ando et al.,KEK Preprint 85 – 15,1985.
η_R				
1275	70	0^{-+}	$\eta\pi^+\pi^-$	N.R. Stanton et al., PRL 42(1979)346.
1280		0^{-+}	$\eta\pi^+\pi^-$	A. Ando et al.,KEK Preprint 85 – 15,1985.

Table 5: The E/ι and η_R mesons.

2.4.2 0^{++} and 2^{++}:

Both nonets are complete if one accepts the assignments [$\delta(980)$, $\epsilon(1300)$, $S^*(990)$, K(1350)] and [$A_2(1320)$, f(1270), f'(1515), K(1430)] respectively. The status of the former nonet is shaky. The δ and S^* are sometimes interpreted as $qq\bar{q}\bar{q}$ molecules, or as $\bar{K}K$ bound states, or as linear combination of these with $q\bar{q}$.

The 2^{++} nonet is in good shape, but the $f \to \eta\eta$ branching ratio would constrain a possible gg component. Glueballs with $J^{PC}=2^{++}$ are predicted in the same mass range, and are likely to appear in $\bar{K}K$, $\eta\eta$ and $\eta\eta'$ channels (if masses allow). The $A_2 \to \eta'\pi$ decay mode, observable in $\bar{p}p \to \pi^{\pm}A_2^{\mp}$ ($A_2^{\mp} \to \eta'\pi^{\mp}$, $\eta' \to \pi^0\pi^0\eta$) would help determine the $\eta-\eta'$ mixing angle and possible gg components in η and η'.

The scanning mode of LEAR can be used to study $\bar{p}p$ formation of 0^{++} and 2^{++} states between 1900 and 2400 MeV. The channels $\bar{p}p \to \pi^0\pi^0$, $\eta\eta$, K_SK_S select only these quantum numbers, and are favourable channels for glueball candidates, (e.g. $\Theta \to \pi^0\pi^0$, $\eta\eta$, $\xi \to K_SK_S$). Measuring these channels simultaneously in one experiment gives a good determination of the branching ratios which are important in deciding if an observed state is a glueball.

2.4.3 $1^{+\pm}$:

The 1^{+-} nonet consisting of [B(1230), H(1190), H'(?), Q_B] is incomplete. The expected mass of the H' is $\approx$1450 MeV. The most likely decay modes are $H' \to \rho\pi$ (OZI suppressed), $H' \to K^*\bar{K}$ (if the mass is higher than 1400 MeV), $H' \to \omega\eta$. The last decay is accessible via $\bar{p}p \to \pi^0H'$ ($H' \to \omega\eta$, $\omega \to \pi^+\pi^-\pi^0$, $\eta \to \gamma\gamma$) or $\bar{p}p \to \pi^+\pi^-H'$ ($H' \to \omega\eta$, $\omega \to \pi^0\gamma$, $\eta \to \gamma\gamma$). The production of H' is suppressed because it is expected to be an $(s\bar{s})$ state. Nonetheless, $\pi^+\pi^-\phi$ is produced with a branching ratio of 2×10^{-4}.

The 1^{++} nonet, on the other hand, has too many candidates, [$A_1(1270)$, D(1285), E(1420), D'(1515), Q_A] The D', fitting nicely into the nonet, is seen in only one experiment[23] and needs confirmation. We could observe it via $\bar{p}p \to \pi^0 D'$ ($D' \to K_S K^+ \pi^-$, $K_S \to \pi^0\pi^0$ or $D' \to \eta\pi^+\pi^-$).

2.5 Radiative Decays of Mesons

Annihilation at rest provides a copious source of meson resonances. Gamma detection offers this experiment the capability of measuring branching ratios of radiative decays, e.g. for ρ, ω, η', ϕ, A_2 and K^* decays to meson + γ, providing backgrounds are manageable. Most of the allowed transitions, as for example between vector and pseudoscalar mesons, are magnetic dipole transitions, and hence the amplitudes measure the quark magnetic moments. Furthermore the amplitudes depend on the quark flavor content of the initial and final mesons, and therefore provide tests of singlet−octet mixing angles. We have the possibility to measure branching ratios for several radiative decays in a single experiment, with many of the mesons appearing in several final states. This offers the possiblity of a significantly overconstrained fit to the relevant mixing angles and magnetic moment parameters.

It is also of considerable interest to search for the radiative decay of the E. Since there is evidence of a radiative decay of the $\iota(1440)$ to $\rho\gamma$, the radiative decay of the E would give additional information relevant to the question of the identity of the two states.

The experimental situation, summarized in Table 6, shows that most of the branching ratios are not well known. SU(3) fitting relies critically on the (large) branching ratio for $\omega \to \pi^0\gamma$. In particular one assumes that the all neutral decay of the ω is exclusively $\pi^0\gamma$. A reduction of the branching ratio is possible if another neutral decay mode with substantial branching ratio (like $\omega \to 3\gamma$ or $\omega \to \pi^0\pi^0\gamma$) is observed [24].

The second column shows data as given in the tables of the Particle Data Group. The third column is a selection from these using additional criteria. In the multiple entries for $\rho \to \eta\gamma$ and $\omega \to \eta\gamma$ all upper values or all lower values must be used since the experimental results are correlated. The fourth column is the prediction of a three-parameter fit to the latter data (Ohshima, 1980). For comparison an earlier, slightly different, prediction is shown in parenthesis (O'Donnell, 1977). The latter prediction also has results for the two-photon decays.

Decay	Experiment: Particle data group	Experiment: Selected (by Ohshima)	SU(3) symmetry	
$\rho \to \pi\gamma$	38 ± 11 keV	67 ± 7 keV	67 ± 7	(65)
$\omega \to \pi\gamma$	889 ± 57 keV	789 ± 92 keV	789 ± 120	(723)
$\phi \to \pi\gamma$	5.7 ± 2.1 keV	6.5 ± 1.9 keV	11.1 ± 14.5	(4.9)
$K^{*0} \to K^0\gamma$	75 ± 35 keV	75 ± 35 keV	147 ± 16	(144)
$K^{*-} \to K^-\gamma$		62 ± 14 keV	37.5 ± 4	(36)
$\rho \to \eta\gamma$	50 ± 13 keV	52.5 ± 13.7 keV	45.6 ± 21.7	(40)
	76 ± 15 keV	79.8 ± 15.9 keV		
$X \to \rho\gamma$	83 ± 30 keV	93.1 ± 25.1 keV	93.1 ± 24.1	(77)
$\omega \to \eta\gamma$	3.0 ± 2.5 keV	3.2 ± 2.6 keV		
		1.9	9 ± 2.5	(6)
	29.0 ± 7.0	30.5 ± 7.4 keV		
$\phi \to \eta\gamma$	62 ± 9 keV	67.7 ± 9.5 keV	137 ± 18	(117)
$X \to \omega\gamma$	7.6 ± 3.1 keV	8.4 ± 2.7 keV	8.4 ± 2.4	(7.5)
$\phi \to X\gamma$			0.7 ± 0.1	(0.5)
$\pi^0 \to \gamma\gamma$	7.86 ± 0.54 eV	7.86 ± 0.54 eV		(7.92 eV)
$\eta \to \gamma\gamma$	323 ± 46.4 eV	323 ± 46.4 eV		(380 eV)
$X \to \gamma\gamma$	5.32 ± 1.98 keV	5.66 ± 1.45 keV		(6.5 keV)

Table 6: Radiative Meson Decays (X = η') (from ref [24]).

2.6 Study of $\bar{p}p$ Annihilation

Final states of two or more mesons can be used to study the $\bar{p}p$ annihilation dynamics. The annihilation process is assumed to be dominated by $q\bar{q}$ annihilation in the $^3S_1$ or $^3P_0$ states. The coupling of $\bar{p}p$ to mesons can be related to meson−nucleon coupling. These questions have been investigated by several authors [25−29].

2.6.1 Annihilation into two Mesons

Since disconnected graphs are forbidden, reactions of the type $\bar{p}p \rightarrow AB(s\bar{s})$, where A and B are non−strange mesons, should be suppressed. Since η and η' are mixtures of $u\bar{u}$, $d\bar{d}$ and $s\bar{s}$, relations are then obtained between $\bar{p}p$ reactions involving the η and η'. Apart from kinematical factors [29]:

$$\sigma(\eta'\eta') = (K/2)\,\sigma(\eta\eta') = K^2\,\sigma(\eta\eta)$$
$$\sigma(\pi^0\eta') = K\,\sigma(\pi^0\eta)$$
$$\sigma(\omega\eta') = K\,\sigma(\omega\eta)$$

where K depends only on the nonet mixing angle α and is independent of the fraction of rearrangement and annihilation type contributions to $\bar{p}p$ annihilation. These two contributions can be obtained by a SU(3) analysis of two meson decays in $\bar{p}p$ at rest [30]. Hence a measurement of any two branching ratios yields α. Recent data on the π^0 and η lifetimes in $\gamma\gamma$ interactions have shifted the value of α to -18 ± 2^0 from the previously accepted $(-8\pm3)^0$ [31].

Additional relations can be obtained if $q\bar{q}$ annihilation dominates quark rearrangement [29]:

$$\sigma(\eta\eta) = a^4\,\sigma(\pi^0\pi^0)$$
$$\sigma(\rho^0\pi^0) = a^2\,\sigma(\omega\eta)$$
$$\sigma(\omega\omega) = \sigma(\rho^0\rho^0)$$

where again a depends only on α. Apart from $\bar{p}p \rightarrow \pi^0\pi^0$ at rest and $\pi^0\pi^0$ ($\pi^0\eta$) above 1 GeV/c [32], the two body neutral channels $\eta\eta$, $\eta\eta'$, $\eta'\eta'$, $\pi^0\eta$, etc have never been isolated. These processes, forbidden at rest from $\bar{p}p$ S states, should be suppressed ($< 10^{-3}$) in liquid hydrogen due to Stark mixing (Day−Snow−Sucher mechanism[33]), but enhanced in hydrogen gas.

2.6.2 Annihilation into three or more Mesons

The comparison of models for $\bar{p}p$ annihilation with experiments has been limited by the lack of experimental data for most of the channels described. Roughly 60 % of the annihilations lead to a final state with more than one neutral (Table 7). Only crude figures for the π^0 multiplicities are known. Channels with more than one π^0 or η have not been studied. The Crystal Barrel experiment will be able to observe most of these channels.

Final state	Branching ratio (%)	
Neutral	4.1 ± 0.4	
$\pi^+\pi^-\pi^0$	6.9 ± 0.4	
$\pi^+\pi^-\pi^0\pi^0$	9.3 ± 3.0	
$\pi^+\pi^-\pi^0\pi^0\pi^0$	23.3 ± 3.0	35.4 ± 0.8
$\pi^+\pi^-\pi^0\pi^0\pi^0\pi^0$	2.8 ± 0.7	
$2\pi^+2\pi^-$	6.9 ± 0.6	
$2\pi^+2\pi^-\pi^0$	19.6 ± 0.7	
$2\pi^+2\pi^-\pi^0\pi^0$	16.6 ± 1.0	20.8 ± 0.7
$2\pi^+2\pi^-\pi^0\pi^0\pi^0$	4.2 ± 1.0	
$3\pi^+3\pi^-$	2.1 ± 0.2	
$3\pi^+3\pi^-\pi^0$	1.9 ± 0.2	

Table 7: Pionic final states in $\bar{p}p$ annihilation at rest (from ref [34]).

Gross features for the multineutral channels can be obtained from the corresponding charged channels through isotopic spin relations. However, the intermediate states are often different. For example, $\bar{p}p \to \omega\pi^0 \to \pi^+\pi^-\pi^0\pi^0$ has no equivalent in $\bar{p}p \to 2\pi^+2\pi^-$. The Dalitz plots for $\bar{p}p \to \pi^0\pi^0\pi^0$ and $\pi^+\pi^-\pi^0$ are also very different [35,36].

2.6.3 Annihilation from Atomic P States

Bubble chamber experiments find little contribution from P state annihilation in liquid hydrogen at rest. The P contribution is usually neglected. Initially the main argument for S dominance comes from the non observation of $\bar{p}p \to K_S K_S$ [37]. Recent data in hydrogen gas [38], where P state annihilation is substantial (P/P+S = 54 ± 12 %), find a strong dynamical suppression of $K_S K_S$ even for P waves. The question on how much P state annihilation contributes in liquid is still open. The channel $\bar{p}p \to \pi^0\pi^0$ is forbidden from atomic S states. A measurement of the branching ratio at rest and in gas would settle this question. The branching ratio in liquid must be remeasured since the two available results $(4.8 \pm 1.0) \times 10^{-4}$ and $(1.4 \pm 0.3) \times 10^{-4}$ disagree [39].

We will study low spin, low mass ($\leq$1700 MeV) states via annihilation at rest, using both a liquid and a gaseous H_2 target. In liquid, antiprotons annihilate predominantly from S states ($^1S_0$ and $^3S_1$); in gas, annihilation occurs from S and P states, but the detection of low energy X−rays (occuring with a rate of 13 ± 2 % [40] per stopped $\bar{p}$) tags P wave annihilations. Selection rules impose marked differences for annihilations from S and P states.

For high mass states the angular momentum barrier is already important for L=2. This is evidenced by the low f production in $\bar{p}p \to f\pi^0$ in liquid (from the $^1S_0$ $\bar{p}p$ state with L=2). The f production is enhanced in gas (from $^3P_1$ or $^3P_2$ with L=1) (Fig. 2). This observation can be generalized.

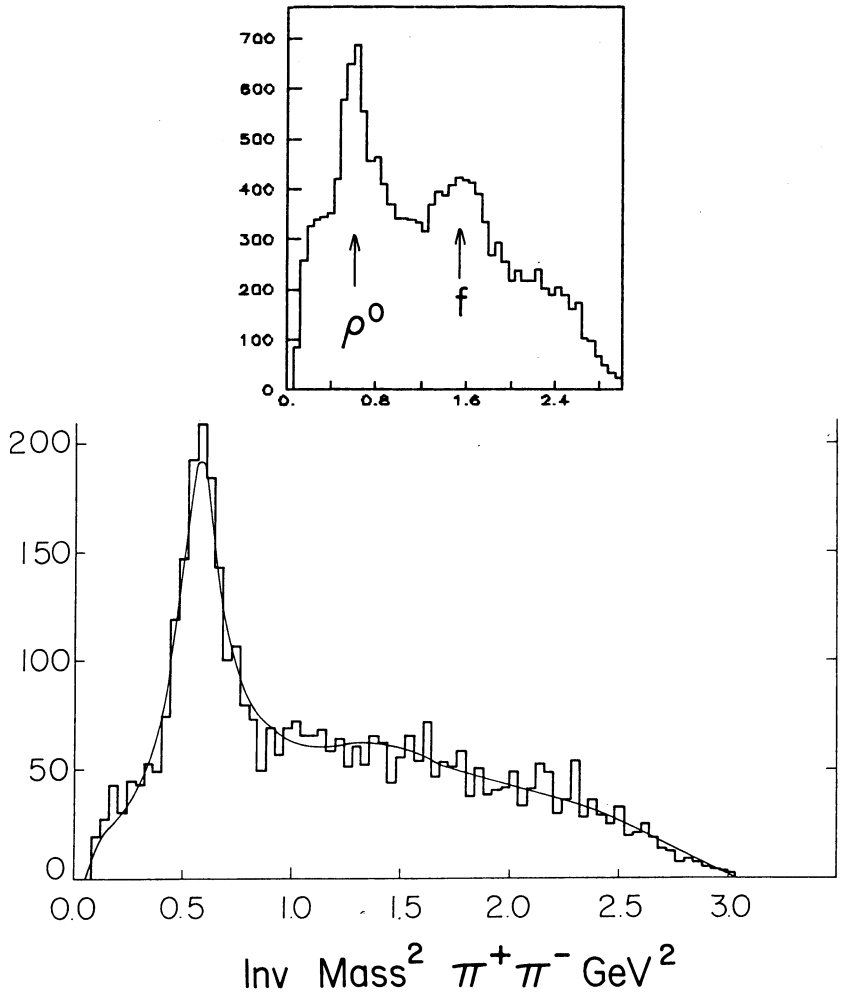

Fig. 2: Invariant $\pi^+\pi^-$ distribution for $\pi^+\pi^-\pi^0$ in gaseous hydrogen (top) [41] and in liquid hydrogen (bottom) [42].

Consider $\bar{p}p \rightarrow \pi^0 X^0$ (A) and $\bar{p}p \rightarrow \pi^+\pi^- X^0$ (B):

1. From S waves if X^0 (channel A) has a high mass and $L=2$ is suppressed, X^0 has 0^{++} or the exotic 1^{-+} in annihilation from $^1S_0$. From $^3S_1$ 1^{--},1^{+-} and 2^{--} are accessible, as well as the exotic 0^{--}. The $\pi^+\pi^-$ pair (channel B) limits the phase space to < 1500 MeV; for high X_0 masses the dipion has no angular momentum and the J^{PC} is restricted to 0^{-+} and 1^{--}.

2. From P waves, X_0 (channel A) is produced with no angular momentum with $J^{PC} = 0^{-+}$, 1^{--}, 2^{-+} and the exotic 1^{-+}. With one unit of angular momentum all states can be produced.

Because of this difference, a comparison of data sets with S wave and P wave annihilations, taken with the same apparatus, will show the presence of a resonance which otherwise may have escaped detection because of large background contributions.

2.7 Search for $\bar{p}p$ Bound States

These states, which are predicted by several models [43], could be observed through π^0 or γ transitions from the $\bar{p}p$ atom. Inclusive gamma spectra have been reported containing narrow structures with yields $\simeq 10^{-3}$ which can be interpreted as evidence for such states [44]. Some models suggest that bound states could be < 10 MeV in width, in which case they can be seen by a high resolution experiment (e.g. the PS183 detector which achieves a γ energy resolution of 3 MeV FWHM between 100 MeV and 300 MeV [45]). If the states are broad, as suggested by other models, then it is necessary to remove the $\pi^0 \rightarrow \gamma\gamma$ background to observe clear signals for the γ transitions. With 95% solid angle coverage and nearly 100% γ detection efficiency, the Crystal Barrel will remove the $\pi^0 \rightarrow \gamma\gamma$ background very effectively, allowing for sensitivities below 10^{-4}. The same sensitivity is expected for radiative decays of mesons.

2.8 Search for $\bar{p}p$ States in Flight

Most experiments measured the total $\bar{p}p$ cross section and the total annihilation cross section. Many partial waves contribute to the $N\bar{N}$ interaction. Consequently small effects are buried in a huge background.

The few exclusive experiments performed thus far show interesting enhancements as a function of energy, for example the channel $\bar{p}p \rightarrow 2\pi^+2\pi^-\pi^0$ (through $\omega\rho$) around 1950 MeV [46] or $\bar{p}p \rightarrow K^+K^-$ around 1935 MeV [47].

The simplest channels are those involving two meson resonances, which are very restrictive on spin and parity. This is especially true for neutral channels (see Table 4). Broad states decaying into two mesons can be studied with phase−shift analyses. The channel $\pi^0\pi^0$ would constrain the analysis of $\bar{p}p \rightarrow \pi^+\pi^-$ presently under study at LEAR by some authors of this proposal (PS172).

In view of the prediction of the flux tube model that hybrids decay preferentially into excited mesons, it seems promising to search for these states in formation by scanning, e.g., $\bar{p}p \rightarrow (\pi D)_{L=1}$ or $(\pi B)_{L=0}$. A hybrid state would show up as a (possibly broad) enhancement in the cross section. The distinctive feature of a hybrid state would then be its strong coupling to excited mesons.

2.9 Typical Channels of Interest

Table 8 shows examples of various intermediate states contributing to specific final states which can be studied by the Crystal Barrel. The brackets in column 3 indicate resonance production. The decay modes of the η, η' and ω are chosen so that the intermediate state decays into the final state given in column 1. The J^{PC} values are derived assuming $L(\bar{p}p)=0$ or $L(\bar{p}p)=1$. Note that some of the intermediate states can also have exotic quantum numbers (see Table 2). There are of course more possible intermediate states (column 3). For example $\pi^0(\eta\eta)$ and $\eta(\pi^0\eta)$ lead to the same final state.

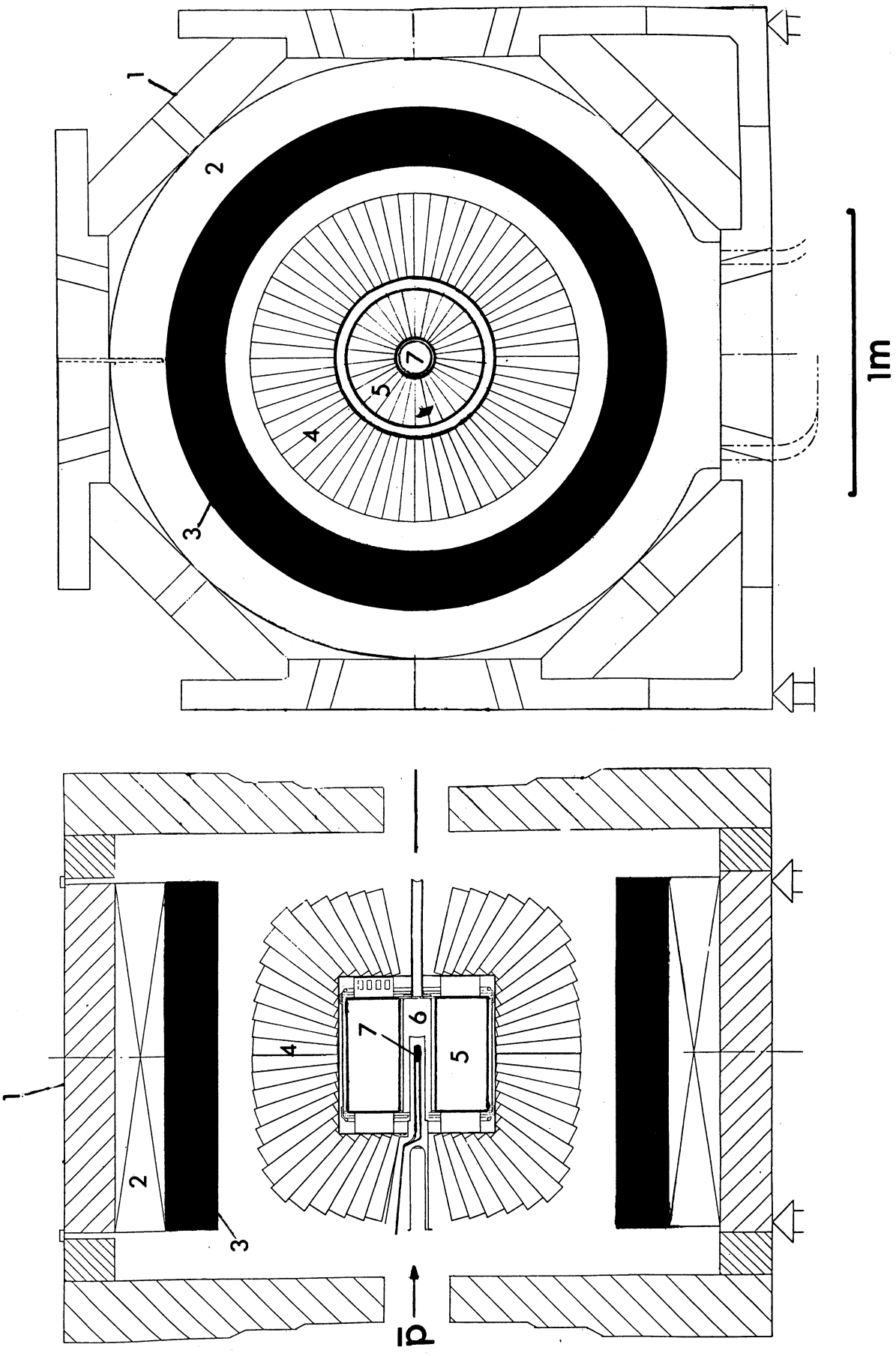

Fig. 3: CB Apparatus: (1) Yoke, (2) Old coil, (3) New coil, (4) CsI barrel, (5) JDC, (6) XDC/PWC, (7) LH_2 target.

4. DETECTOR PERFORMANCE

4.1 Charged Particle Detection

The transverse momentum of charged particles will be measured by the JDC between $\theta = 18^0$ and 162^0 with respect to the beam axis. The solid angle for best resolution is 63% 4π ($51^0 < \theta < 129^0$). Prototype tests for the L3 detector and at SLAC show that a position resolution of $\sigma = 50\mu$ can be achieved at 1 atm with a CO_2 – Isobutane mixture. Diffusion in the gas will deteriorate the resolution to 65μ for the maximum drift space of 2.5 cm. With a less optimistic figure of 100μ we will achieve the momentum resolution shown in Fig. 4 (32 samplings, 1.5 T and track lengths of 18.6 cm). Below 200 MeV/c the resolution is dominated by multiple scattering in the chamber. The resolution is roughly a factor of two better than in the ASTERIX experiment (PS171) [48].

With a solid angle coverage of 99% 4π (JDC and XDC) we will track charged particles between 8^0 and 172^0. The coordinate along the beam axis will be determined by charge division with a resolution $\sigma_z = 4$ mm. This leads to an angular resolution of better than 10 mrad over the whole angular range. The resolution on the direction of charged particles is better than 1^0. The annihilation vertex for charged events will be measured with an rms precision of 1 mm.

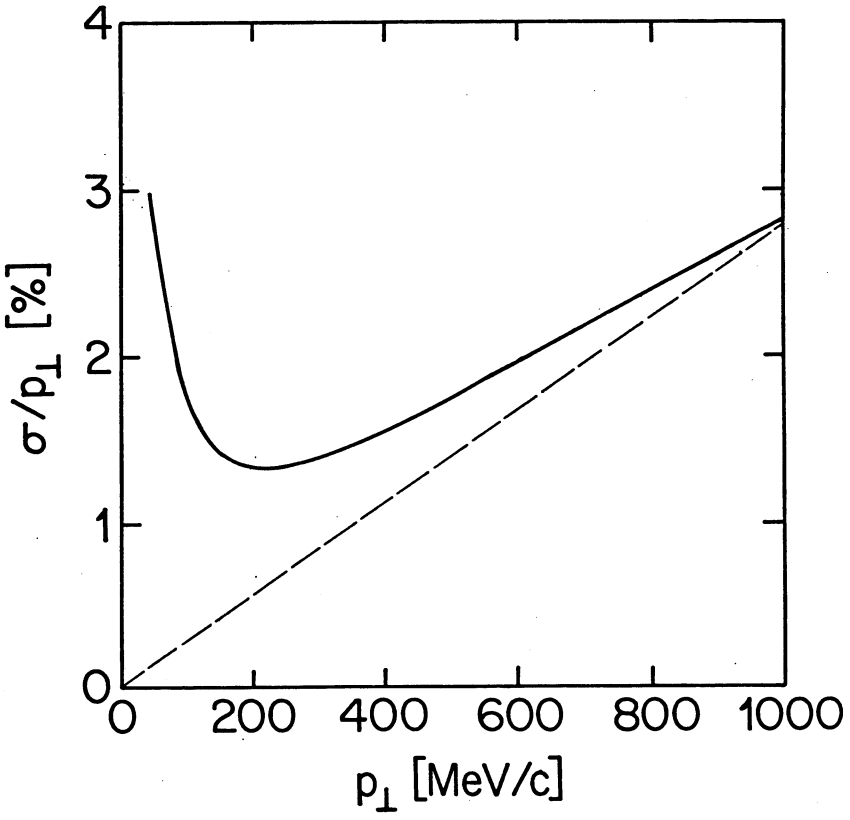

Fig. 4: Momentum resolution for charged pions.
Dashed line: $\sigma/p = 0.028$ p [GeV/c].

Low energy charged kaons can be separated from charged pions in the JDC by dE/dx up to 500 MeV/c . The ASTERIX experiment achieves 35 % FWHM dE/dx resolution in an Argon/Ethane drift chamber (Fig.5). With 32 samples the JDC should lead to an improved dE/dx resolution of 23 % FWHM. Between 500 and 1000 MeV/c K^+/π^+ separation is possible by measuring the energy loss in the CsI barrel (Fig.6). This method does not work very well for negative particles due to nuclear interactions.

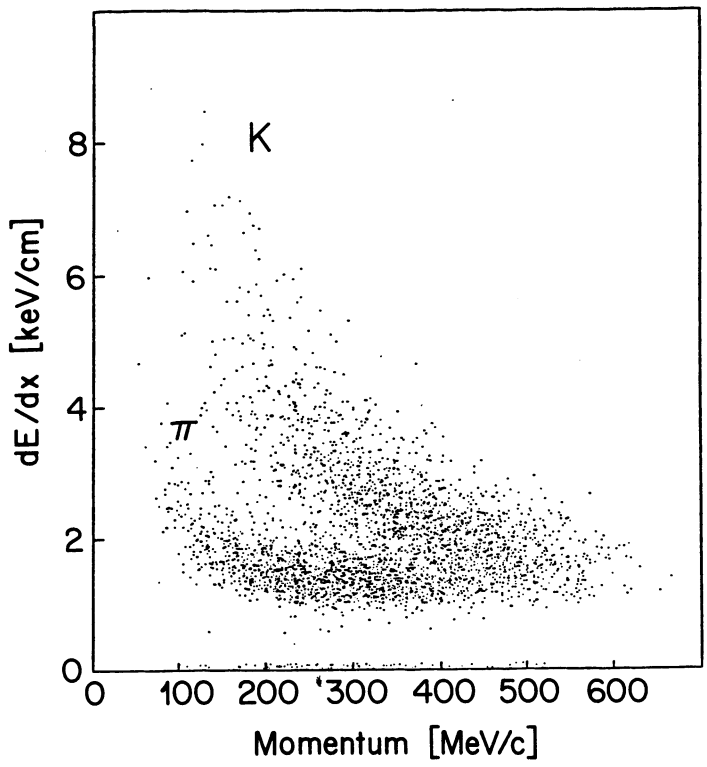

Fig. 5: dE/dx π/K separation in the ASTERIX experiment.

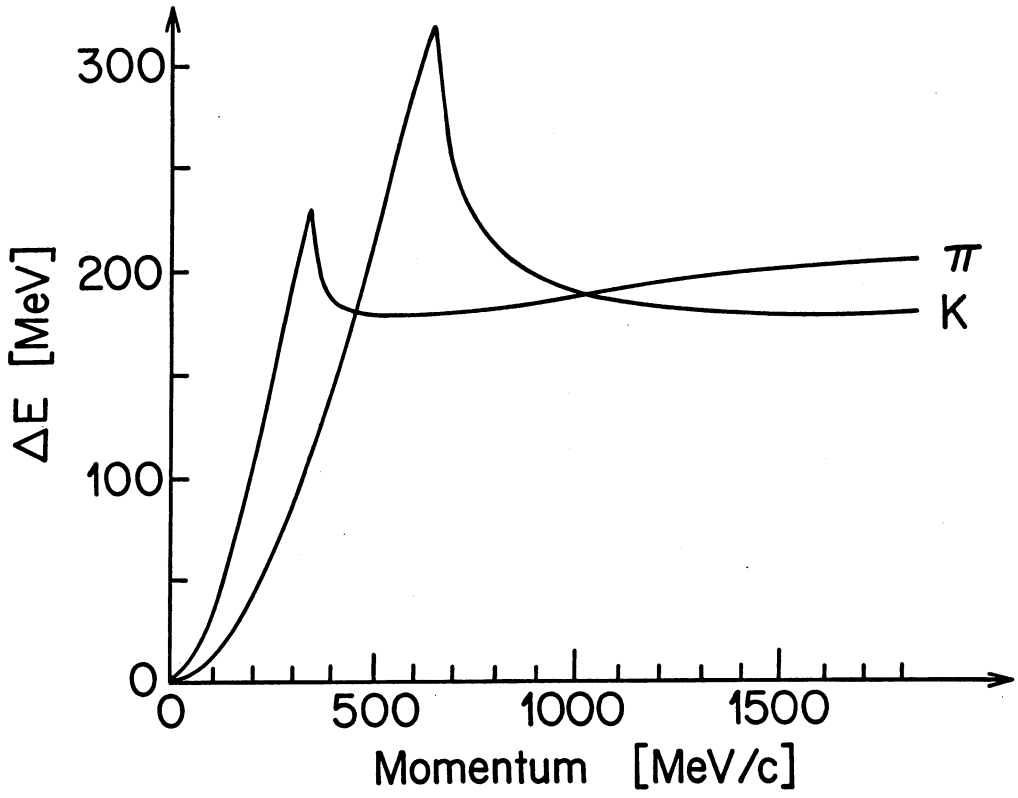

Fig. 6: Energy loss in the CsI barrel for pions and kaons.

The decay $K_S \to \pi^+\pi^-$ has a typical decay length of 2 cm. Using momentum measurements in the JDC we can reconstruct the K^0 mass with a σ of 4 MeV. The fact that the vertex resolution is much smaller than the K_S decay length means that for channels with a K_S and additional charged particles we can use the decay impact parameters to identify the K_S. For K_S momenta above 200 MeV/c 5 – 20 % of the K_S decays occur within the sensitive volume of the XDC or PWC, thus allowing a fast multiplicity trigger on K_S (Fig.7).

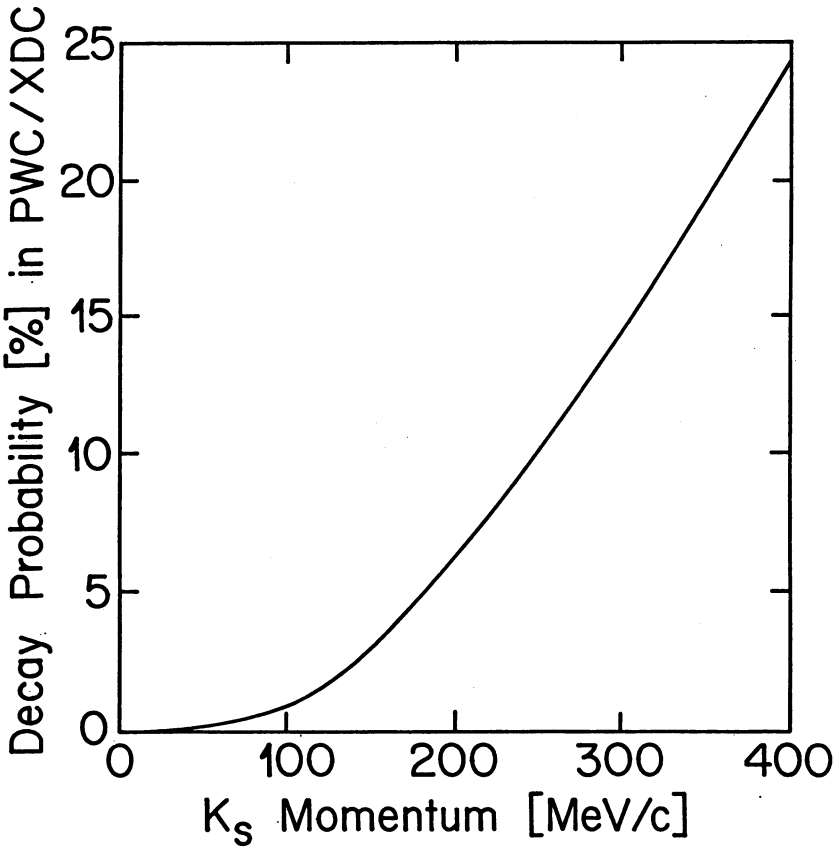

Fig. 7: Probability for $K_S \to \pi^+\pi^-$ in the XDC or PWC ($\bar{p}p \to K_S K\pi\pi$ at rest).

The long–lived neutral kaons will not decay inside the spectrometer but can still be identified by missing mass since they are the only particles (other than ν's) which are not detected by either the JDC or the barrel. The K_L missing mass resolution has a σ of 18 MeV. A significant fraction of the K_L interact in the crystals. These interactions will add constraints to the fit of the event since the K_L direction is measured.

At 2 GeV/c incident $\bar{p}$ momentum annihilation particles tend to move into the forward hemisphere. Fig. 8 shows the angle θ of the π^+ versus the angle of the π^- in $\bar{p}p \to \pi^+\pi^-\pi^0$. The boxes indicate the angular range covered by the JDC. For most events one particle traverses the JDC while the second moves forward with a reduced track length in the JDC. Events with higher multiplicities are more uniformly distributed. This effect, together with the higher average momentum, leads to a worse momentum resolution for charged particles. The resolution improves however substantially if kinematical fitting is applied, our events being fully reconstructed. Table 9 gives the mass resolutions for different annihilation channels at 2 GeV/c. The figures quoted are obtained with all events for which all charged particles enter the JDC.

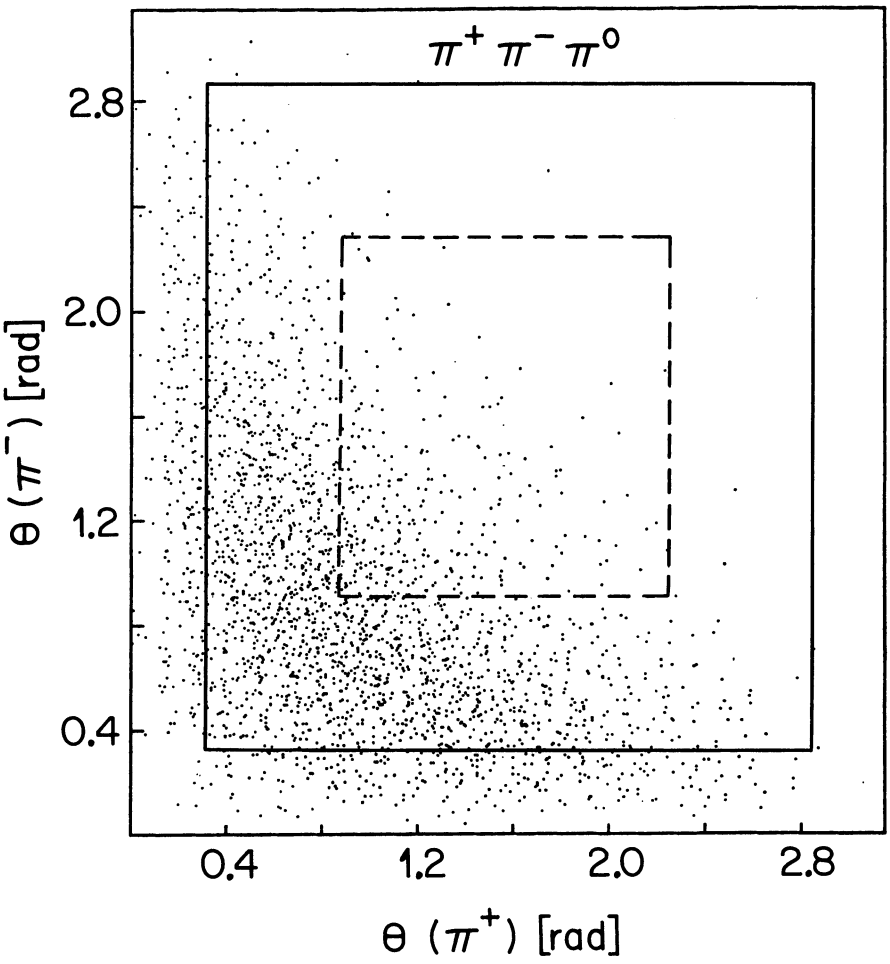

Fig. 8: $\theta(\pi^+)$ vs $\theta(\pi^-)$ in $\bar{p}p \to \pi^+\pi^-\pi^0$ (2 GeV/c).
The solid line shows the angular coverage of the JDC, while the dashed line shows the region of best resolution for both pions.

Channel	Mass	700 MeV	1400 MeV	2100 MeV
$\pi^+\pi^-\pi^0$	$m(\pi^+\pi^-)$	21	27	21
$\pi^+\pi^-3\pi^0$	$m(\pi^+\pi^-)$	21	28	
$\pi^+\pi^-2\pi^0$	$m(\pi^0\pi^0)$	35	37	
$2\pi^+2\pi^-\pi^0$	$m(\pi^+\pi^-\pi^0)$	23	42	

Table 9: Invariant mass resolutions at 2 GeV/c (FWHM in MeV).

4.2 Neutral Particle Detection

For the performance of the CsI Crystal Barrel we rely on past experiences with the Stanford NaI Crystal Ball [49] and with the 54 module NaI sector operated by several members of the present collaboration [50]. Extensive investigations have also been made for the CsI barrel of the CLEO II project [51]. In addition we have studied the γ detection efficiency, and angular and energy resolutions with the EGS shower code[52].

The 1380 barrel modules will cover a solid angle of 97.8 % 4π. Due to shower loss in the tunnel modules (beam entrance and exit) the tunnel modules will only be used as veto counters. The solid angle is thus reduced to 95 % 4π. The corresponding Crystal Ball figures are 93 % and 85 % respectively. Each Crystal Barrel module covers 6^0 in θ and 6^0 in ϕ. In the forward and backward regions ($\theta < 24^0$, $\theta > 156^0$) the angular range in ϕ increases to 12^0. This leads to resolutions of $\sigma_\theta = 30$ mrad and $\sigma_\phi = 30$ (60) mrad which we adopt for all simulations. These figures are overestimated since the angles will be computed with improved accuracy from the shower centroids using adjacent modules. Fig. 9 shows σ_θ as a function of γ energy for the Stanford Crystal Ball obtained by centroid calculations. The radiation lengths of CsI and NaI are 1.9 and 2.6 cm respectively. The lateral shower size is reduced in CsI by roughly 1.4. Correspondingly, our granularity is increased with 1380 modules compared to 720 for the Crystal Ball. Since our cavity radii are comparable we should reach an angular resolution of $\sigma_\theta = 20$ mrad above 200 MeV. EGS calculations are in excellent agreement with this prediction (Fig.9).

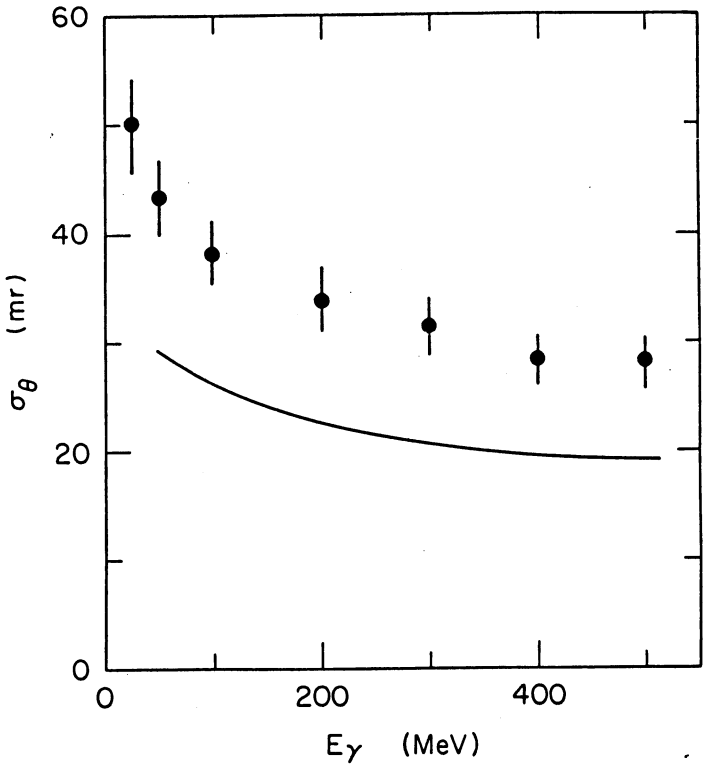

Fig. 9: σ_θ vs γ energy in the Stanford Crystal Ball (data points from ref [49]) and EGS prediction for 3 cm wide CsI modules, 27 cm from the photon source (full curve).

The γ energy resolution obtained by the Crystal Ball is

$$\sigma/E = \alpha / (E\,[\mathrm{GeV}])^{1/4} \quad (\alpha = 0.026)$$

Blüm et al [50] obtain $\alpha = 0.014$ with their 54 NaI sector. Our EGS calculations for CsI give $\alpha = 0.017$ for the sum of 25 adjacent modules and 0.023 for the sum of 9 adjacent modules in excellent agreement with similar calculations performed for CLEO II [51]. The central module contains 70 % of the γ energy. We adopt the realistic figure of

$$\sigma/E = 0.020/ (E[\mathrm{GeV}])^{1/4}$$

eg. 3.5% at 100 MeV.

The resulting π^0 and η mass resolutions are shown in Fig. 10. At high momenta the mass resolution is determined by angular resolution while at low momenta it is dominated by energy resolution. For π^0 detection in our energy range good angular resolution is essential, while for η detection good energy resolution is crucial. Fig. 11 shows the momentum resolution for π^0 and η derived with the constraining fit

$$m^2\ (\pi^0 \text{ or } \eta) = 2E_1E_2(1-\cos\psi)$$

where ψ is the angle between the two photons.

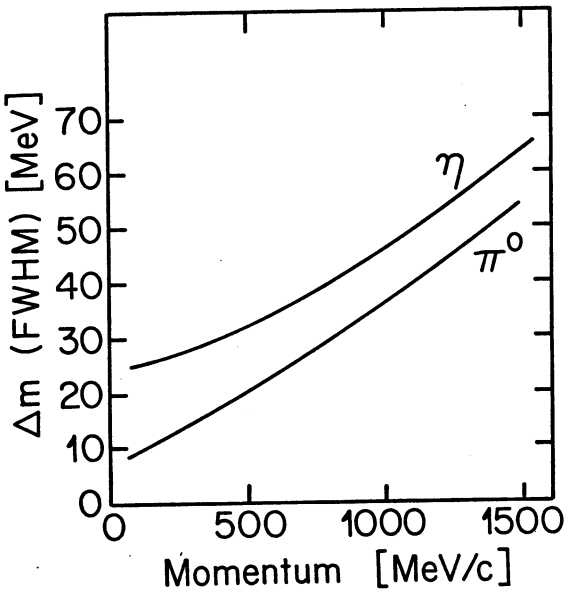

Fig. 10: Mass resolution (FWHM) for π^0 and η.

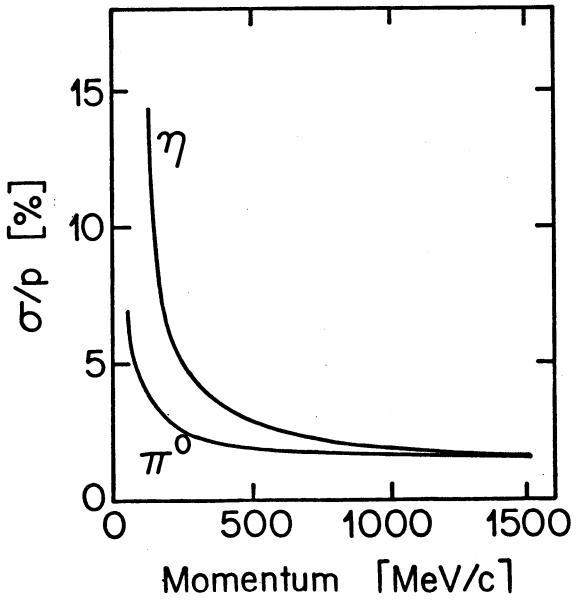

Fig. 11: Momentum resolution for π^0 and η.

Charged particles usually fire one to two CsI modules. The effect of magnetic field bending is negligible. Extensive Monte Carlo calculations by the Crystal Ball group show that 42 % of the energy deposit stems from primary ionization, 45 % from knocked out protons, secondary π^0 and μ's from π and K decay, and 13 % from nuclear split offs. Comparison with data shows however that the contribution from nuclear split offs is overestimated[49].

With 16 radiation lengths the γ detection efficiency is 100 %. Interference with charged particles and shower overlaps reduce the efficiency in a complicated way that depends on the final state multiplicity and on the reconstruction algorithm. For best energy resolution the Crystal Ball sums 13 adjacent (triangular) modules and requires a minimum separation of 32° between central modules from charged and neutral particles (Fig. 12a). Their detection efficiency has been computed in the decay $\psi' \rightarrow \gamma\chi$ [49]. The average final state multiplicity is eight. The average γ detection efficiency is 70% including 85 % 4π solid angle coverage. A further efficiency drop is due to relatively poor charged particle detection in the central detector of the Crystal Ball leading to confusion between neutral and charged particles, good separation then requiring extensive shower pattern cuts. Because of our better granularity and the shorter radiation length we will be able to reduce the separation cut to 23°. A cut of 18° corresponds to summing 9 adjacent modules, a cut of 30° to summing 25 adjacent modules (Fig. 12b). With our increased solid angle of 95 % 4π the average effective γ detection efficiency is then 89 % for $\bar{p}p$ annihilation at rest and 72 % at 2 GeV/c (see Table 10, column 5). These figures can be improved on by relaxing the 23° cut and thus sacrifying slightly on the energy resolution. For low energy γ's we will sum 25 modules. For high energy photons (> 1 GeV) the sum of 9 is sufficient.

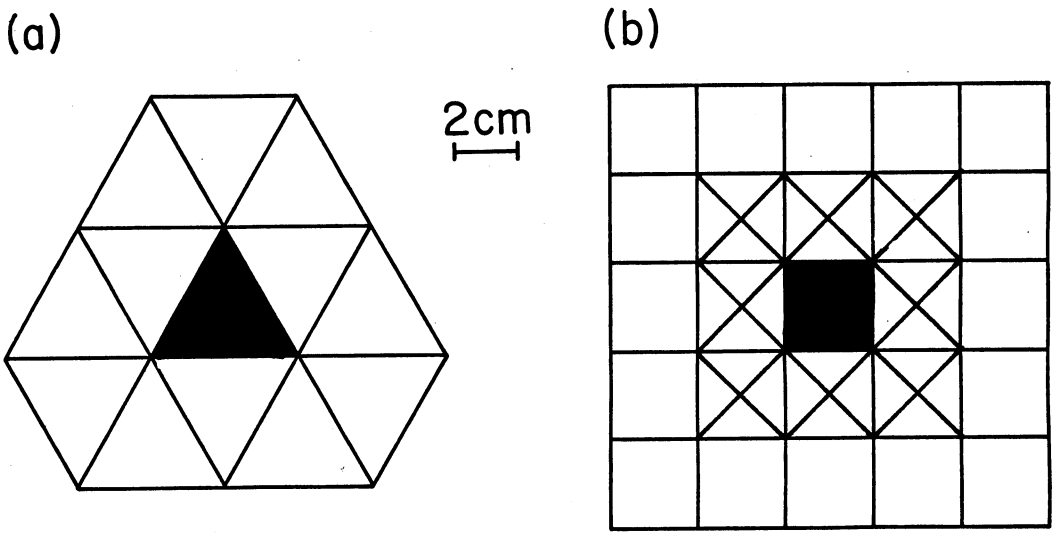

Fig. 12: Sum of 13 modules in the Crystal Ball (a) and sum of 9 and 25 modules in Crystal Barrel (b).

As the momentum increases the reconstruction of π^0's becomes difficult since the photons cluster around a small opening angle ψ_0. The Crystal Ball reconstructs easily π^0's up to 750 MeV ($\psi_0 = 17.5^0$). Our better granularity will allow us to reach 1250 MeV ($\psi_0 = 12.4^0$). The reconstruction of π^0's up to 2 GeV is nevertheless possible by studying the shower profiles. A Monte Carlo study evaluating the reconstruction of high energy π^0's has been done[53]. Fig. 13a gives the effective mass distribution obtained by assuming the π^0 hypothesis for showers produced by single photons. Fig. 13b gives the corresponding distribution for showers produced by π^0's. A clear separation is observed even for 2 GeV π^0 energy. For all simulations we assume the (pessimistic) upper limit of 1250 MeV π^0 energy.

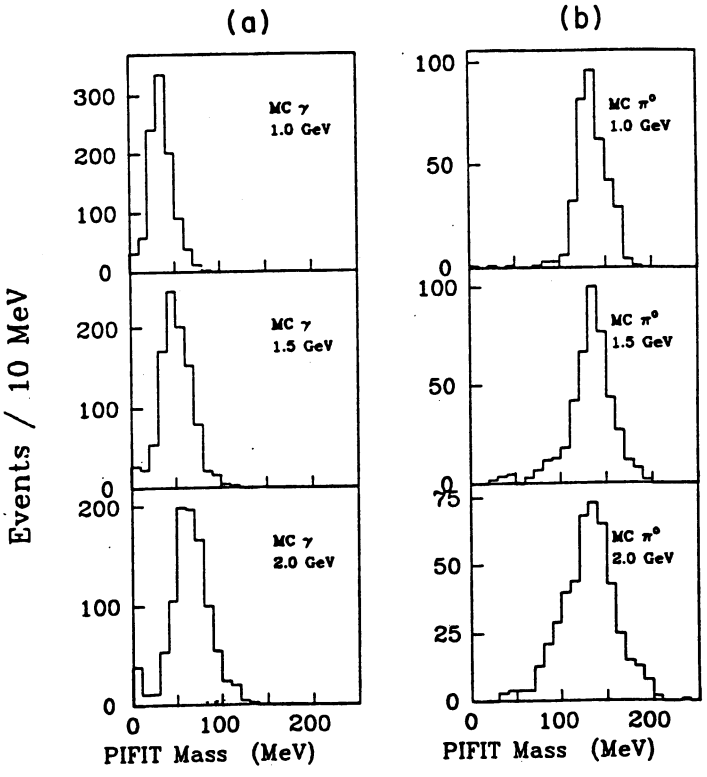

Fig. 13: $\gamma\gamma$ mass distribution for Monte Carlo γ's(a) and π^0s(b) at various energies computed from shower profiles in the Stanford Crystal Ball (from ref [53]).

4.3 Simulations

Since annihilation channels are fully reconstructed, the contribution from background channels with higher final state neutral multiplicities is negligible. Also in general a final state can be suitably chosen for which the combinatorial background is much reduced.

Fig. 14 shows the distributions of the missing mass recoiling against $\pi^+\pi^-$ and $2\pi^+2\pi^-$ in 2 prong and 4 prong annihilations (data sample from ASTERIX). Signals from the missing π^0, η, ω (or ρ) are clearly visible over the large background from final states with more than one neutral π^0. In the 4 prong data the peak is due to $\bar{p}p \to 2\pi^+2\pi^-$ and the tail to final states with more than one π^0. The Crystal Barrel measures the π^0 and η decays which are missing in previous experiments, making it possible to study exclusive final states with negligible background (Table 10). For annihilation at 2 GeV/c we assume the same branching ratios as for annihilation at rest. A π^0 (η) is reconstructed whenever the $\gamma\gamma$ invariant mass falls within the windows 110 to 160 MeV (500 to 600 MeV). For ω reconstruction the $\pi^0\gamma$ mass should lie between 750 and 810 MeV. Kinematical fitting (energy and momentum conservation) is applied. Column 4 gives the probability to reconstruct an event (including solid angle and detection efficiency). Column 5 gives the effective γ detection efficiency, including the 23^0 cut in cluster separation. The main background contribution (column 6) stems from events with missing photons. The background to signal ratios given in column 8 are much smaller than those obtained in bubble chamber experiments or previous counter experiments (e.g. ASTERIX). The larger background at 2 GeV/c comes from the higher particle density in the forward hemisphere and from the 1250 MeV cut on the π^0 energy.

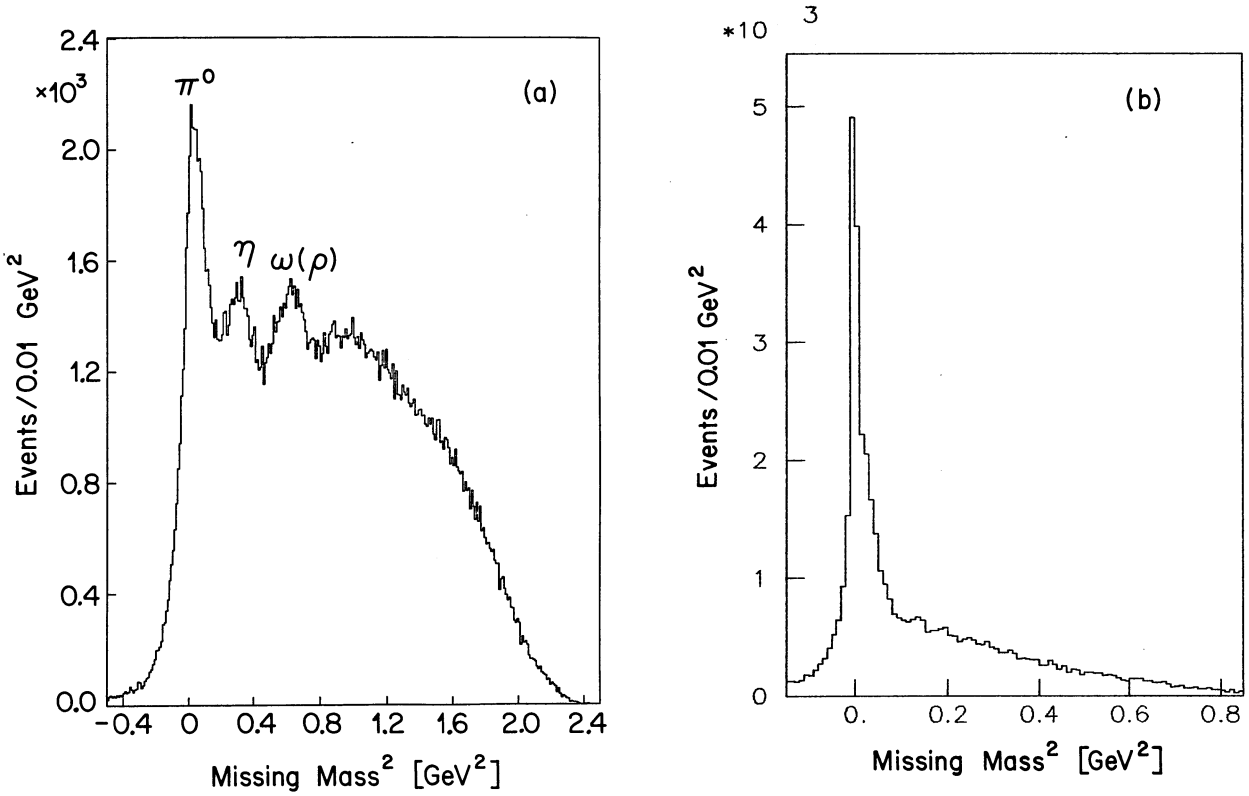

Fig. 14: Missing mass recoiling against $\pi^+\pi^-$ in 2 prong events (a) and against $2\pi^+2\pi^-$ in 4 prong events (b) (data from PS171).

Channel	p [GeV/c]	BR [%]	Eff [%]	γ Eff [%]	Back-ground	BR [%]	R
$\pi^+\pi^-2\pi^0$	0	9.3	64	90	$\pi^+\pi^-3\pi^0$	23.3	9.0×10^{-3}
	2		24	74			3.2×10^{-2}
$2\pi^+2\pi^-2\pi^0$	0	16.6	46	84	$2\pi^+2\pi^-3\pi^0$	4.2	1.0×10^{-3}
	2		15	70			1.9×10^{-2}
$\pi^+\pi^-\pi^0$	0	6.9	85	94	$\pi^+\pi^-2\pi^0$	9.3	2.0×10^{-4}
	2		41	71			2.5×10^{-3}
$\pi^+\pi^-\eta$	0	0.44	84	94	$\pi^+\pi^-2\pi^0$	9.3	1.0×10^{-2}
	2		62	87			9.5×10^{-2}
$2\pi^+2\pi^-\eta$	0	0.28	69	87	$2\pi^+2\pi^-2\pi^0$	16.6	$< 10^{-2}$
	2		34	75			2.6×10^{-1}
$2\pi^+2\pi^-\pi^0$	0	19.6	71	88	$2\pi^+2\pi^-2\pi^0$	16.6	2.0×10^{-4}
	2		32	73			5.6×10^{-3}
$\pi^+\pi^-\omega$	0	0.26	74	92	$\pi^+\pi^-2\pi^0$	9.3	5.2×10^{-2}
$(\omega \rightarrow \pi^0\gamma)$	2		43	83			0.92

Table 10: Detection efficiency and background contribution R for various channels (see text).

4.3.1 Neutral Final States

We have investigated the performance of the Crystal Barrel for the channels $\bar{p}p \rightarrow \pi^0\pi^0\pi^0$, $\pi^0\pi^0$, $\pi^0\eta$ and $\eta\eta$ (which are sensitive probes of the annihilation dynamics) at rest and up to 2 GeV/c. The vertex of neutral events can be reconstructed with a resolution of typically 1.4 cm FWHM (Fig. 15). The data sample will therefore be free of background from beam interaction outside the target.

For two body final states the angular distribution can be measured from 20^0 to 160^0 in the cms frame. The reconstruction efficiency is typically 80%. The background for the channel $\bar{p}p \rightarrow \pi^0\pi^0$ is from the reaction $\bar{p}p \rightarrow 3\pi^0$ and $2\pi^0\eta$, each of which have a branching ratio of about 1 % [36]. In the Crystal Barrel the background to signal ratio is much less than 1 % and the counting rate for the channel at rest in liquid is 48 (14) events/s at 10^5 $\bar{p}$/s using the branching ratios reported in [39]. We will clearly resolve the discrepancy between the previous measurements.

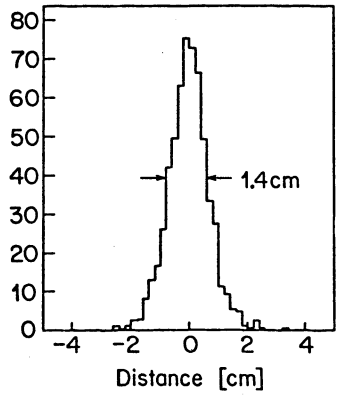

Fig. 15: Vertex resolution for $\bar{p}p \rightarrow 3\pi^0$ at 500 MeV/c.

We have estimated the rate for $\bar{p}p \rightarrow \pi^0\pi^0$ for an incident flux of 10^5 $\bar{p}$/sec as a function of beam momentum (Table 11) using

$$\sigma(\pi^0\pi^0) = (38 + 35/ p\,[\mathrm{GeV/c}]) \times 3.7 \times 10^{-3} \times 0.4$$

where the term in brackets describes the total annihilation cross section. The branching ratio for $\bar{p}p \to \pi^+\pi^-$ at rest is 3.7 x 10^{-3} [54]. This branching ratio is also approximately valid above 1 GeV/c [55]. The channels $\pi^0\pi^0$ and $\pi^0\eta$ have been measured above 1 GeV/c [32]. The $\pi^0\pi^0/\pi^+\pi^-$ ratio is about 0.4. The rate for $\pi^0\eta$ should be 30 % lower (extrapolating from the data above 1 GeV/c). The branching ratio for $\bar{p}p \to \eta\eta$ is unknown. The background rejection is better than 5 x 10^{-6} / BR($\bar{p}p \to \eta\eta$).

p [MeV/c]	$\pi^0\pi^0$ rate [s^{-1}]	Background [s^{-1}]
300	4	< 0.04
500	3	< 0.03
900	2	0.02

Table 11: $\bar{p}p \to \pi^0\pi^0$ rates for 10^5 $\bar{p}$/s

4.3.2 Glueballs

We have simulated the channel $\bar{p}p \to E\pi^+\pi^-$ ($E \to \eta\pi^0\pi^0$) in which the E is a glueball candidate. Since the branching ratio for this channel is unknown, we estimate it from the known branching ratio for $E\pi^+\pi^-$ ($E \to K_S K\pi$) of 7 x 10^{-4} [54]. The E is known to decay 50 % via K^*K and 50 % via $\delta\pi$ [56]. The relative branching ratio R = $(\delta \to \eta\pi)/(\delta \to K\bar{K})$ is not known. It is unclear why the $\delta \to \eta\pi$ is observed in the D $\to \delta\pi$ decay and not in the $E/\iota(1440) \to \delta\pi$ decay. The final state $E \to \eta\pi^0\pi^0$ is however observed at high energies [57]. With a 40 % branching ratio for $\eta \to \gamma\gamma$ and R $\simeq$ 3.4 from D decay, we arrive at a branching ratio of 2.4 x 10^{-4} for the channel $\bar{p}p \to E\pi^+\pi^-$ ($E \to \delta^0\pi^0$, $\delta^0 \to \eta\pi^0$, $\eta \to \gamma\gamma$). The main background contribution comes from $\pi^+\pi^-\pi^0\pi^0\eta$ (possibly via $\delta^0\pi^0$), the branching ratio of which we assume to be 2.8 x 10^{-3} by comparison with the already observed $2\pi^+2\pi^-\eta$ [54].

Events are simulated for $\bar{p}p$ annihilation at rest assuming phase space distributions. The E mass is 1420 MeV and its width 50 MeV. The δ cut is 929 < m($\eta\pi$) < 1037 MeV. Events are submitted to kinematical fitting. The resulting $\delta^0\pi^0$ mass spectrum is shown in Fig.16. The detection efficiency for the channel $E\pi^+\pi^-$ ($E \to \eta\pi^0\pi^0$) is 25 %. The background contribution from $\bar{p}p \to \pi^+\pi^-3\pi^0$ is negligible. The channel $\bar{p}p \to E\pi^0\pi^0$ ($E \to \eta\pi^+\pi^-$) leads to the same final state and looks similar. The clear identification of these channels could distinguish between the E and the ι observed in e^+e^- experiments.

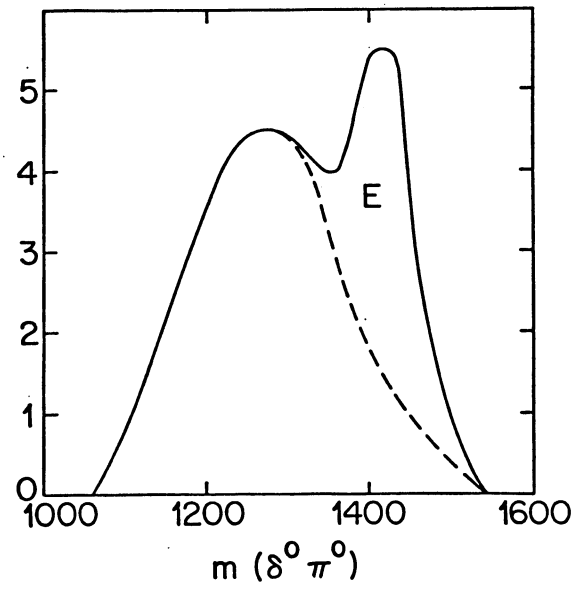

Fig. 16: $\delta^0\pi^0$ invariant mass distribution in $\bar{p}p \to E\pi^+\pi^-$ at rest ($E \to \delta^0\pi^0$, $\delta^0 \to \eta\pi^0$). The dashed curve shows the background from $\bar{p}p \to \eta\pi^+\pi^-\pi^0\pi^0$.

4.3.3 Hybrids

We have simulated at 2 GeV/c the channels

A) $\bar{p}p \rightarrow \pi^{\pm}X^{\mp}$, $X^{\mp} \rightarrow D\pi^{\mp}$, $D \rightarrow \delta^0\pi^0$, $\delta^0 \rightarrow \eta^0\pi^0$
leading to the final state $\pi^+\pi^-\pi^0\pi^0\eta$

B) $\bar{p}p \rightarrow \pi^{\pm}X^{\mp}$, $X^{\mp} \rightarrow B^0\pi^{\mp}$, $B^0 \rightarrow \omega\pi^0$, $\omega \rightarrow \pi^0\gamma$
leading to the final state $\pi^+\pi^-\pi^0\pi^0\gamma$ The X is one of the hybrids predicted by Isgur et al.[19] Its mass is assumed to be 1900 MeV and its width 30 MeV in channel A, 100 MeV in channel B.

The background channels contributing to channel A are:

1. $\bar{p}p \rightarrow X^0\pi^0$, $X^0 \rightarrow D\pi^0$, $D \rightarrow \delta^{\pm}\pi^{\mp}$, $\delta^{\pm} \rightarrow \eta\pi^{\pm}$

2. $\bar{p}p \rightarrow \pi^+\pi^-D$, $D \rightarrow \delta^0\pi^0$, $\delta^0 \rightarrow \eta\pi^0$

3. $\bar{p}p \rightarrow \pi^0\pi^0D$, $D \rightarrow \delta^{\pm}\pi^{\mp}$, $\delta^{\pm} \rightarrow \eta\pi^{\pm}$

4. $\bar{p}p \rightarrow \pi^0\pi^0\pi^+\pi^-\eta$

Channel 1 is the kinematical reflexion of channel A for a neutral X. The channel $\pi^+\pi^-D$ ($D \rightarrow K_SK\pi$) has been measured at 730 MeV/c [58]. The branching ratio is 4×10^{-4} of the annihilation cross section, which we also take for 2 GeV/c. The corresponding ratio for $D \rightarrow \delta^0\pi^0$ should be 6.5×10^{-4} which, with $\eta \rightarrow \gamma\gamma$, leads to a branching ratio of 2.6×10^{-4}. We assume that the channels $X^{\pm}\pi^{\mp}$ contribute 10^{-4}. For channel 4 we take 2.8×10^{-3} as in 4.3.2.

Phase space distributions are assumed in the center of mass reference frame. The simulated events are submitted to kinematical fitting. The δ mass cut is $927 < m(\eta\pi) < 1037$ MeV and the D cut $1240 < m(\delta\pi) < 1330$ MeV. Channels 1 and 3 have a negligible contribution due to the D cut. The resulting $D\pi^{\pm}$ mass distribution is shown in Fig. 17a. The detection efficiency for the channel A is about 10 %. The channel $\bar{p}p \rightarrow \pi^0X^0$ looks similar.

The background channels contributing to channel B are:

1. $\bar{p}p \rightarrow X^{\pm}\pi^{\mp}$, $X^{\pm} \rightarrow B^{\pm}\pi^0$, $B^{\pm} \rightarrow \omega\pi^{\pm}$

2. $\bar{p}p \rightarrow \pi^+\pi^-B^0$, $B^0 \rightarrow \omega\pi^0$

3. $\bar{p}p \rightarrow \pi^{\pm}\pi^0B^{\mp}$, $B^{\mp} \rightarrow \omega\pi^{\mp}$

4. $\bar{p}p \rightarrow \pi^+\pi^-\pi^0\omega$

5. $\bar{p}p \rightarrow \pi^+\pi^-3\pi^0$

Channel 1 is the kinematical reflexion of channel B for a charged B meson. Contribution 5 requires that one of the γ's is outside the acceptance of the crystals. When cuts are made on total energy−momentum balance and the ω mass this contribution is found to be negligible. The ω mass cut is $730 < m(\pi^0\gamma) < 830$MeV and the B mass cut is $1080 < m(\omega\pi^0) < 1380$. The larger width of the B meson makes the background contributions from channels 1,3 and 4 more significant than for the D meson channel.

Information on the yields of channels 2−4 is not available from bubble chamber data because of the presence of two π^0s in the final state. The yield of $\omega\pi^+2\pi^-$ is measured to be 1.3 % at 2 GeV/c [59], but no information is available on B meson production. From the ratio of $B^{\pm}\pi^{\mp}$ to $\omega\pi^+\pi^-$ at rest [54], we estimate a yield of 3×10^{-3} for channels 2+3. The $\omega \rightarrow \pi^0\gamma$ decay fraction of 8.7 % reduces the yields of channels 2+3 to 2.5×10^{-4}, and channel 4 to 1.1×10^{-3}. We once again assume that channels $X^{\pm}\pi^{\mp}$ contribute 10^{-4}. With these yields we obtain the $B^0\pi^{\pm}$ mass distribution shown in Fig. 17b.

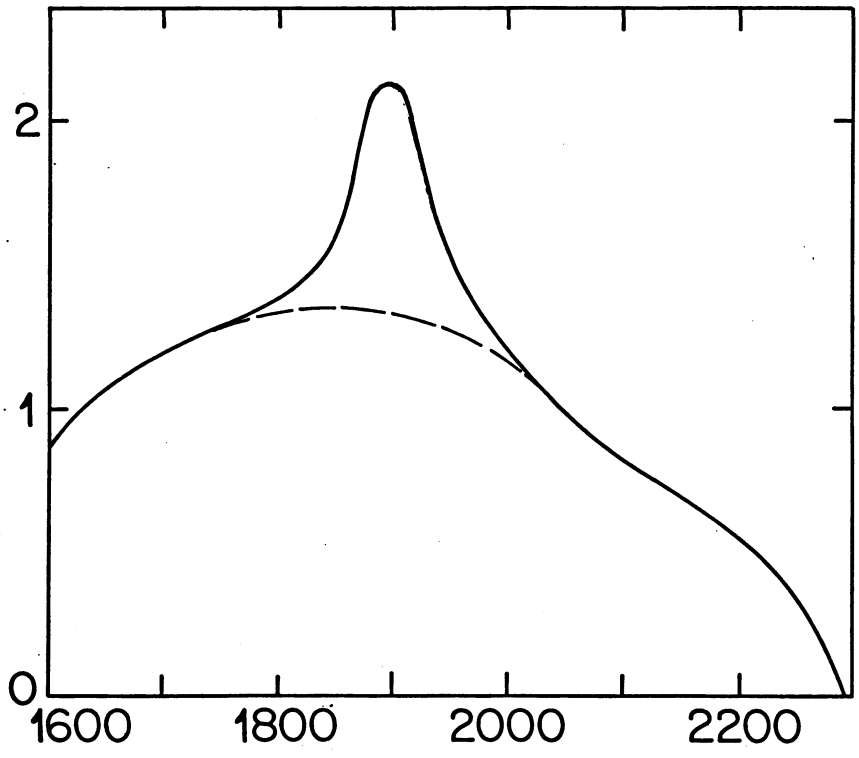

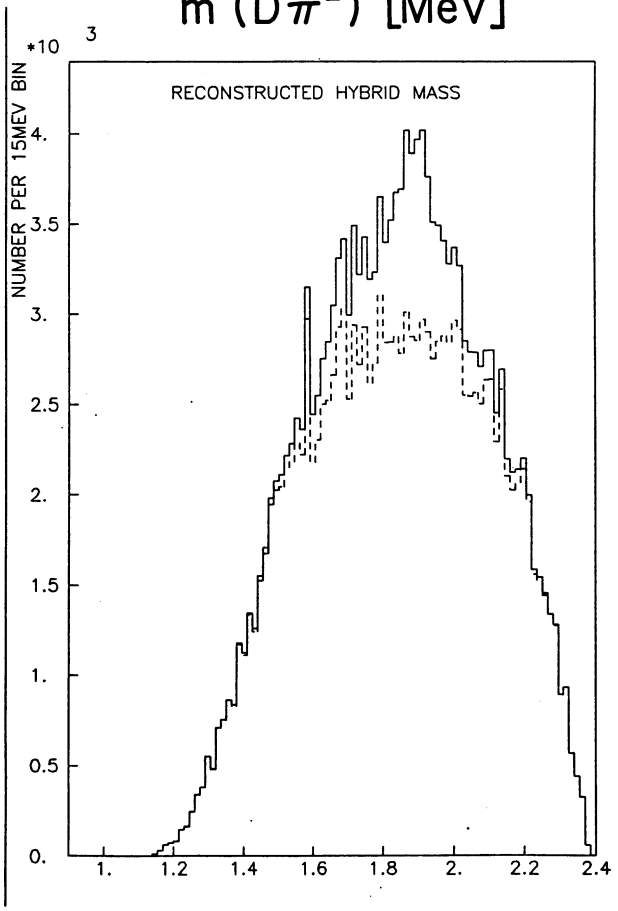

Fig. 17: a) $D\pi^{\pm}$ invariant mass distribution in $\bar{p}p \rightarrow X^{\pm}(1900)\pi^{\mp}$, ($X^{\pm} \rightarrow D\pi^{\pm}$, $D \rightarrow \delta^0\pi^0$, $\delta \rightarrow \eta\pi^0$).
b) $B^0\pi$ mass distribution in $\bar{p}p \rightarrow X(1900)^{\pm}\pi^{\mp}$ $X^{\pm} \rightarrow B^0\pi^{\pm}$, $B^0 \rightarrow \omega\pi^0$, $\omega \rightarrow \gamma\pi^0$.
The dashed lines show the background.

4.3.4 γ Transitions in Exclusive Channels.

To investigate the performance of the Crystal Barrel for radiative transitions we consider the reaction $\bar{p}p \rightarrow \gamma X$ where X are hypothetical narrow states. For illustration purposes we use the states reported earlier in $\bar{p}p$ annihilation at rest [44]. The yields for the narrow states X associated with γ transitions are 9×10^{-4} (1210 MeV), 10^{-3} (1383 MeV), 6×10^{-4} (1421 MeV), 3×10^{-3} (1638 MeV) and 1.6×10^{-3} (1694 MeV). In addition we select the final state $X \rightarrow \pi^+\pi^-\pi^0$ with an assumed branching ratio of 20 %.

The background is simulated by phase space distributions of the outgoing pions and the known charged and neutral pion multiplicities (Table 7). The main background comes from $\pi^+\pi^-2\pi^0$ with only three photons detected. Total momentum and energy conservation is applied. The result is shown in Fig. 18. With 100 hours of LEAR beam time we achieve sensitivities of the order 3×10^{-5} for $\bar{p}p \rightarrow \gamma X$, $X \rightarrow \pi^+\pi^-\pi^0$. The sensitivity does not depend strongly on the decay mode of the states.

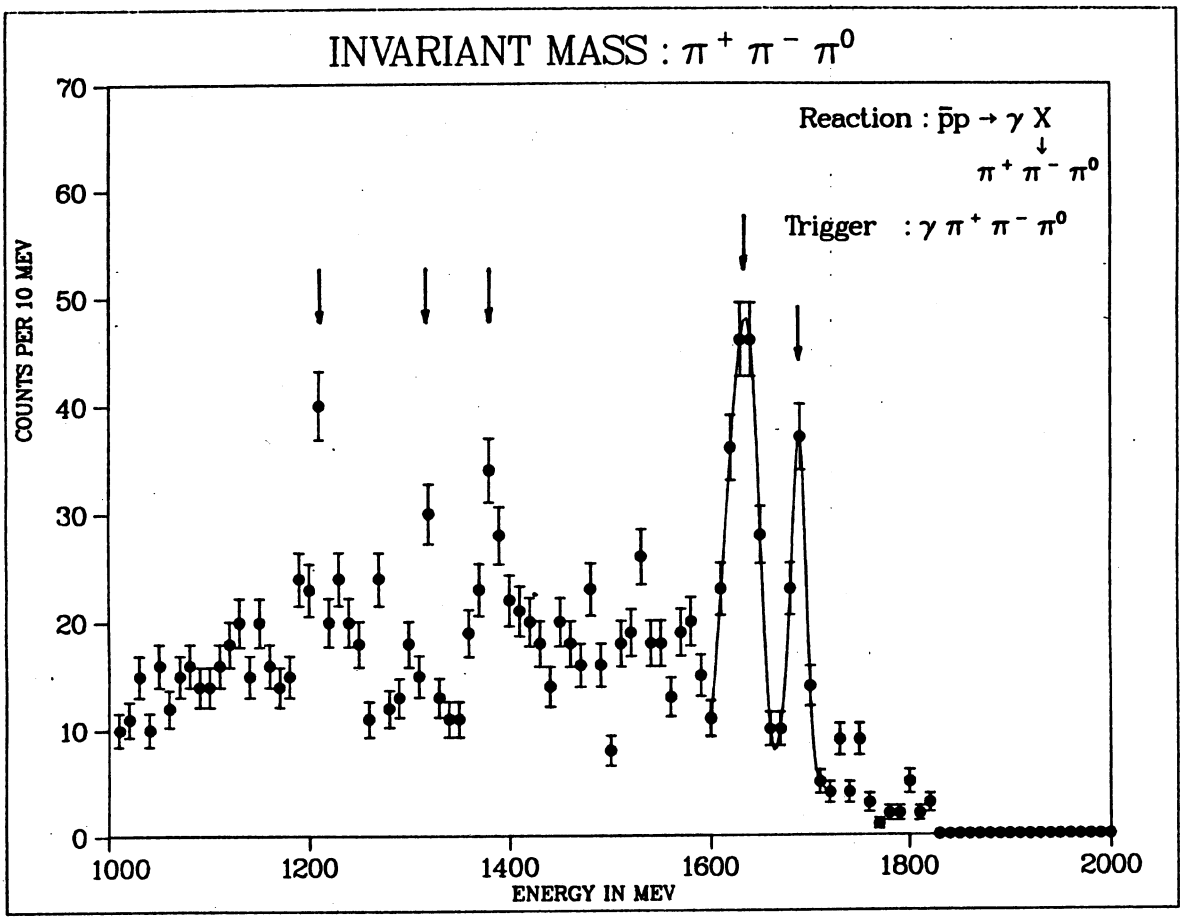

Fig. 18: Simulation of γ transitions associated with narrow states. The assumed branching ratios are given in the text.

5. APPARATUS DESCRIPTION

5.1 Magnet

We will use the DM1 magnet loaned by the Laboratoire de L'Accélérateur Linéaire (LAL – Orsay). This magnet, now used by the ASTERIX collaboration in the N2 zone, could be left in its present position. Together with the already available experimental barrack this would represent a substantial savings in time and installation costs.

The field of DM1 is now 0.8 T. A copper solenoid will be added inside the present aluminium coil to provide a field of 1.5 T. The two coils will be connected in parallel from a single power supply. The power requirements are 500V and 5000A. The inner diameter of the new coil is 140 cm and its length 125 cm.

Due to field saturation additional shielding will be necessary to eliminate the fringe field. This will be achieved by mounting steel plates 5 cm thick around the magnet, leaving an air gap of a few cm. Calculations show that the field will be homogeneous: within the JDC volume the field varies by less than 2 % (Fig. 19).

The above considerations are preliminary and will be pursued in detail by engeneering staff at our laboratories and CERN. Technical specifications and costs will be available soon.

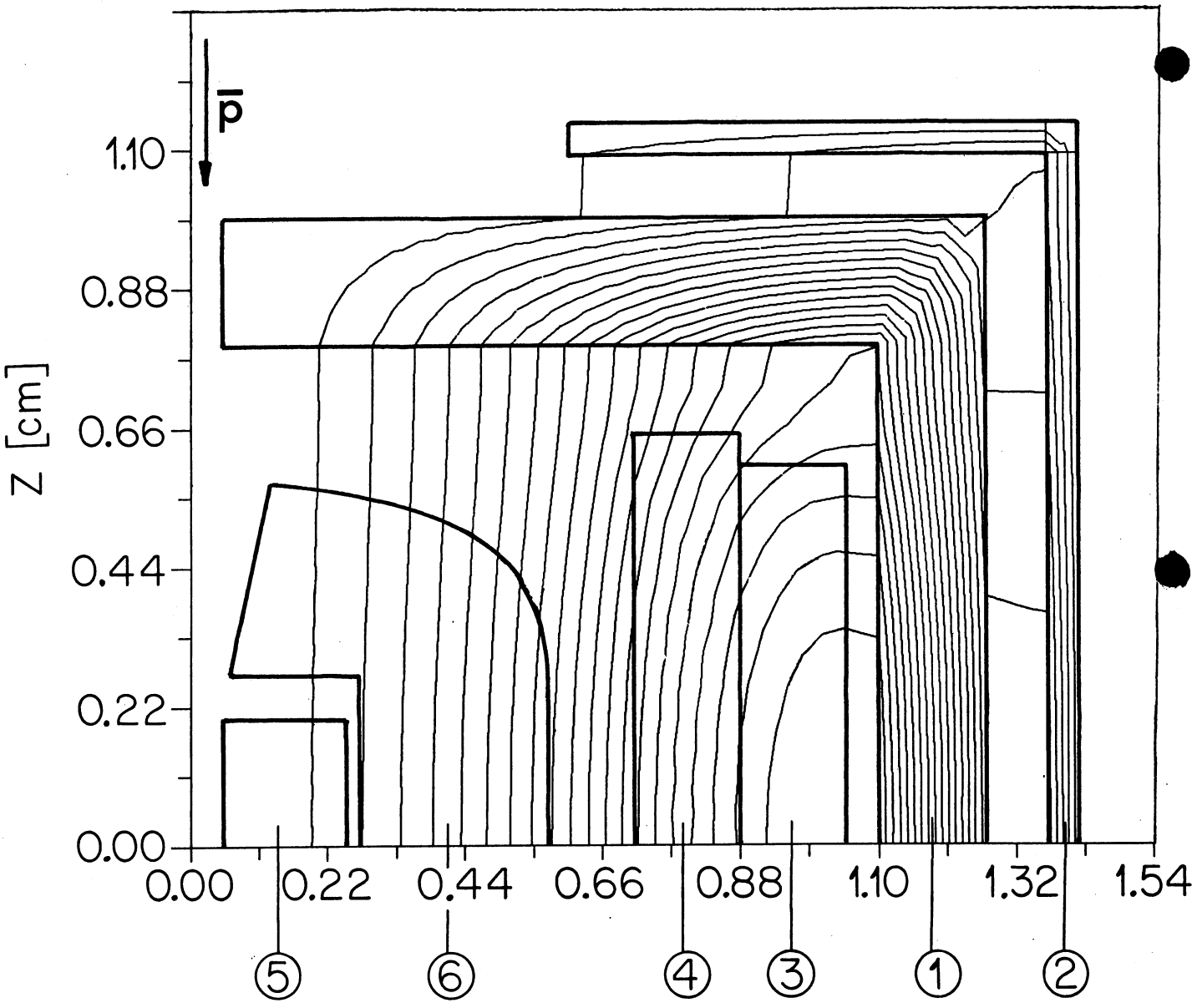

Fig. 19: Magnetic field calculations for the modified DM1: (1) Yoke, (2) Shielding, (3) Old coil, (4) New coil, (5) JDC, (6) CsI Barrel.

5.2 Liquid Hydrogen Target

Annihilation with initial angular momentum L = 0 (atomic S states) will be studied with a liquid hydrogen target. The liquid hydrogen target (Fig.20) is 4 cm long and 15 mm in diameter. The LEAR vacuum ends at a beryllium window approximatively 230 mm upstream of the target center. A thin plastic scintillator ($\leq$ 500μm) located downstream of the window counts individual beam particles. The multiple scattering of the window and scintillator gives a beam size of 1 cm FWHM at the target center for stopping interactions. The spot size for in flight events is smaller.

These specifications were discussed with L. Mazzone and his group. The liquid hydrogen target will be constructed at CERN.

5.3 Cylindrical Multiwire Proportional Chambers (PWC)

This chamber will be a cylindrical proportional wire chamber consisting of two anode layers at radii of 25 mm and 43 mm. Its purpose is to obtain the event multiplicity, to solve rate dependent multitrack ambiguities in the JDC, and to permit a fast trigger on K_S decay by detecting a multiplicity change between the inner and outer layers. While the PWC gives a rough measurement in the $r-\phi$ plane ($\pm$ 1 mm), the longitudinal coordinate z measurement by charge division will be better than those available from the JDC since the PWC wire multiplication will be higher.

The design shown in Fig. 21 has 80 and 128 wires in the two anode layers with a pitch of 2 mm. The wires are read out at each end to provide vertex information by the charge division technique. The inner and outer shells are made of concentric cylinders of RESOFIL (10^{-4} radiation length). The active length is 350 mm.

A prototype will be constructed for the PS183 experiment in 1986 and the triggering capability for K_S evaluated.

5.4 X-Ray Drift Chamber (XDC)

Annihilation with initial angular momentum L = 1 (atomic P states) will be studied with a gas target by detecting L X-rays. The yield of L X-rays in H_2 gas at NTP is 13 $\pm$ 2 % [40]. From the 2p state the $\bar{p}p$ system annihilates with 98 % probability [40]. With the proposed XDC (Fig. 22), the probability to detect an L X-ray is about 5 %. As explained below a fast trigger on L X-rays will be used to select P state annihilation.

The PWC/LH_2 target will be replaced by the XDC. Antiprotons of 100 MeV/c enter a 30 cm long H_2 gas target through a thin mylar window. The width of the range curve for a momentum bite of 10^{-3} is about 4 cm, so that most $\bar{p}$ stop in the target. The separation between the H_2 gas and the chamber gas is achieved by a 6 μ thin aluminized mylar membrane transparent to X-rays with energies > 500 eV. The X-rays are converted in the argon/ethane gas of the XDC. The charge drifts to the anode wires (36 wires strung parallel to the beam axis at a radius of 4.3 cm). The high voltage is supplied by the aluminized mylar membrane (radius 2 cm). The conversion point is determined by the anode wires (ϕ) and by charge division (z). We will use flash ADC's to digitize the drift time and pulse heights (VME electronics used by UA1 and PS171).

Charged particles can be distinguished from X-rays by their characteristically long pulse shape. Also, X-rays usually fire only one signal wire, while traversing prongs generate clusters of several wires. This feature allows a fast X-ray trigger: X-rays are selected by requiring a hit on a single wire with no hits on adjacent wires. The trigger efficiency is 90 %, e.g. 90 % of the events written to tape are actually associated with atomic X-rays detected in the XDC. The fraction associated with an actual L X-ray is 50 % in the offline analysis.

These requirements have already been achieved with the XDC used by PS171.

5.5 Jet Drift Chamber (JDC)

Information about charged particles produced in annihilation events will be obtained with a high resolution cylindrical drift chamber placed inside the crystals. With a spatial resolution of 100 μm (σ) for each of 32 measurements of a track coordinate (r/ϕ), we will obtain resolutions between 1.5 % and 3 % (σ) for transverse momenta between 100 MeV/c and 1 GeV/c (see Fig. 4). In addition we will use pulse height measurements to separate charged pions and kaons for momenta below 500 MeV/c. The z coordinates of tracks will be measured by charge division on the wires with a precision of 4 mm.

The chamber design parameters are summarised in Table 12, and an isometric view of the chamber is shown in Fig. 23. The wires are strung between 6 mm thick aluminium endplates which are supported at the outer edge by a 3 mm thick aluminium cylinder, and at the inner edge by a 300 μm thick carbon fibre reinforced plastic cylinder. Aluminium is used in preference to a lighter material because it is easy to machine and has good electrical and heat conduction properties. The maximum amount of material for photon conversion on the outside of the chamber is 10 % of a radiation length.

The chamber is supported by a 4 cm diameter, 3 mm thick stainless steel pipe which attaches to the barrel support via the 12 cm hole in the downstream side of the crystals. Around the pipe are placed the signal cables, gas and high voltage supplies.

The wire configuration is that of the jet chamber (JADE,OPAL)[60], with 30 radial sectors being used to keep drift times short, and allow for rapid association of charged tracks with signals in the crystals. Fig. 24 shows an end view of the chamber, while Fig. 25 shows the detailed design of a sector. In each sector there are 32 layers of sense wires at a spacing of 6 mm, with a guard wire placed between each layer to focus drift electrons and adjust the gain on the sense wires. A 6 mm sense wire spacing is chosen to give good spatial resolution and sufficient redundancy in sampling. The sense wires will be staggered by $\pm$ 200 μm to resolve the left/right ambiguity. Around each sector, field shaping wires are placed at 3 mm spacing to define a uniform drift field. The chamber will be operated at a gain of 5 x 10^4 with a drift field of 1 kV/cm.

Inner radius	50 mm
Outer radius	270 mm
Sensitive length	400 mm
Innermost sense wire radius	62 mm
Outermost sense wire radius	248 mm
Number of sectors	30
Number of layers	32
Layer thickness	6 mm
Number of wires:	
Sense	960
Guard	990
Field	2400
Sense wire diameter	20 μm
Sense wire material	Stainless steel
Field wire diameter	150 μm
Field wire material	Gold plated aluminium
Average drift field	1 kV/cm
Sense wire gain	5 x 10^4
Gas	CO_2 – Isobutane (90:10)
Pressure	1 Atm
Average drift velocity	8.5 μm/ns
Maximum drift time	3 μs
Lorentz angle at 1.5 T	7.2^0
Amount of material:	
Carbon fiber inner cylinder	0.002 rad. lengths
Aluminium outer cylinder	0.035 rad lengths
Aluminium endplates and electronics	0.1 rad. lengths

Table 12: JDC properties

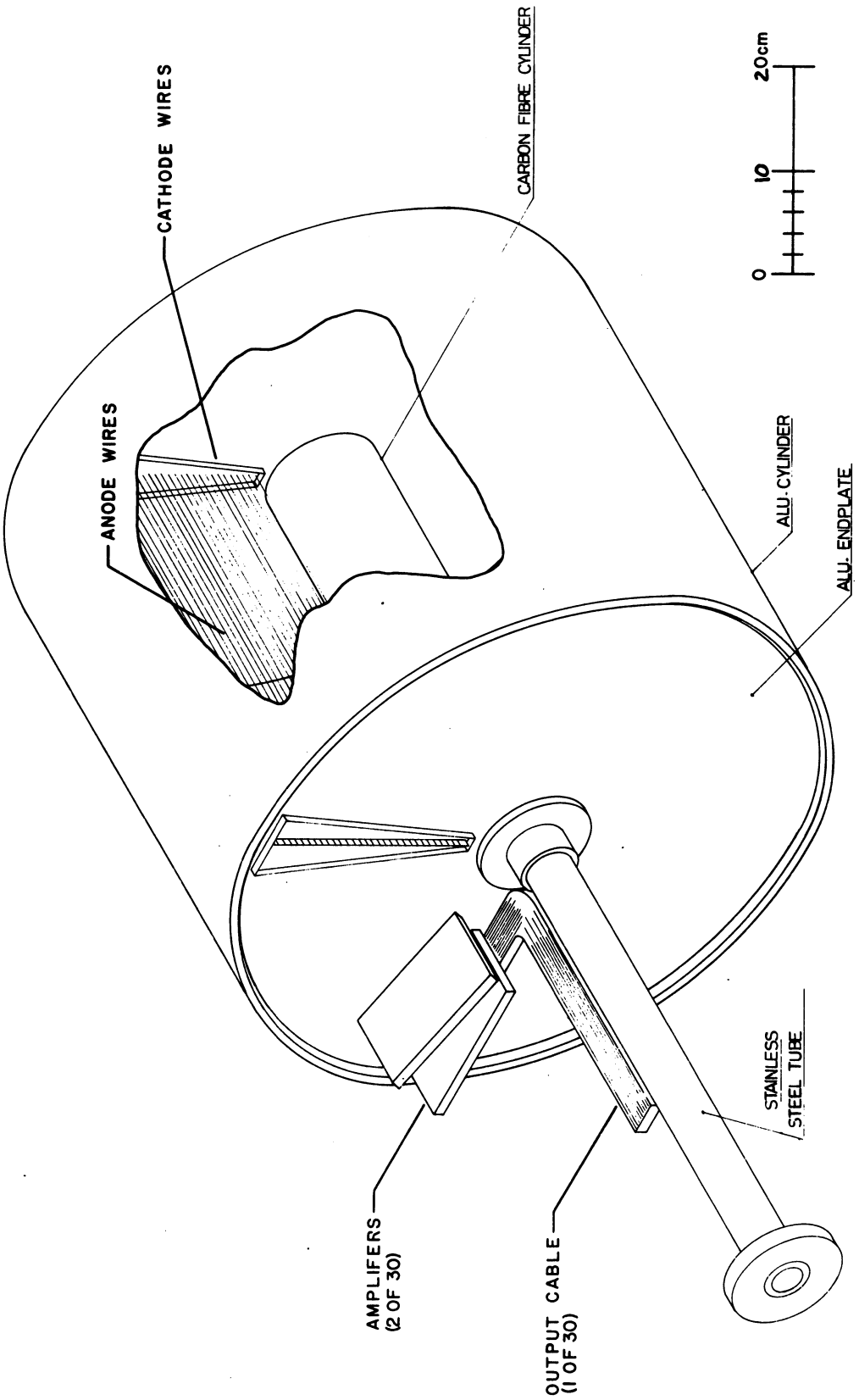

Fig. 23: Isometric view of the Jet Drift Chamber (JDC).

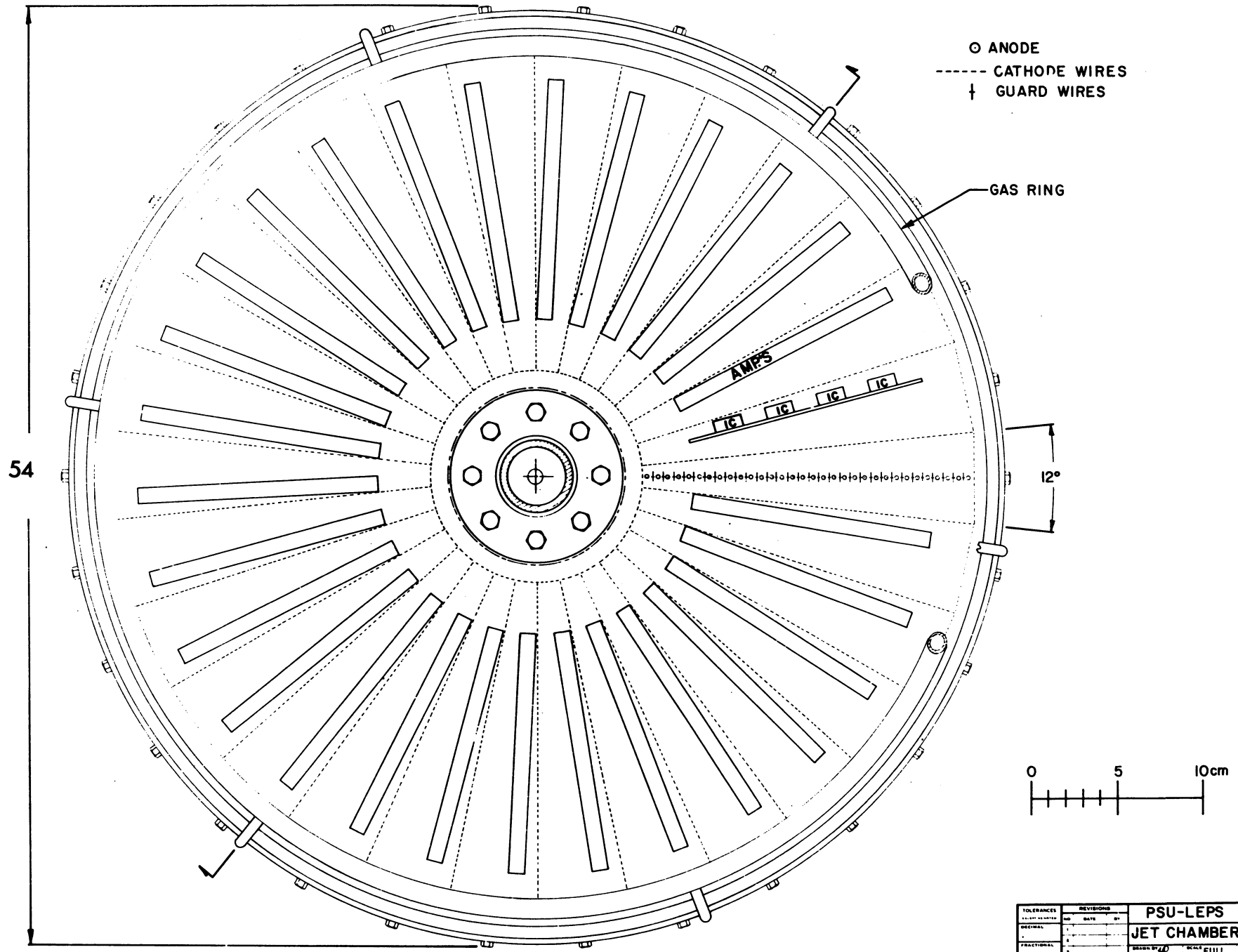

Fig. 24: End view of the JDC.

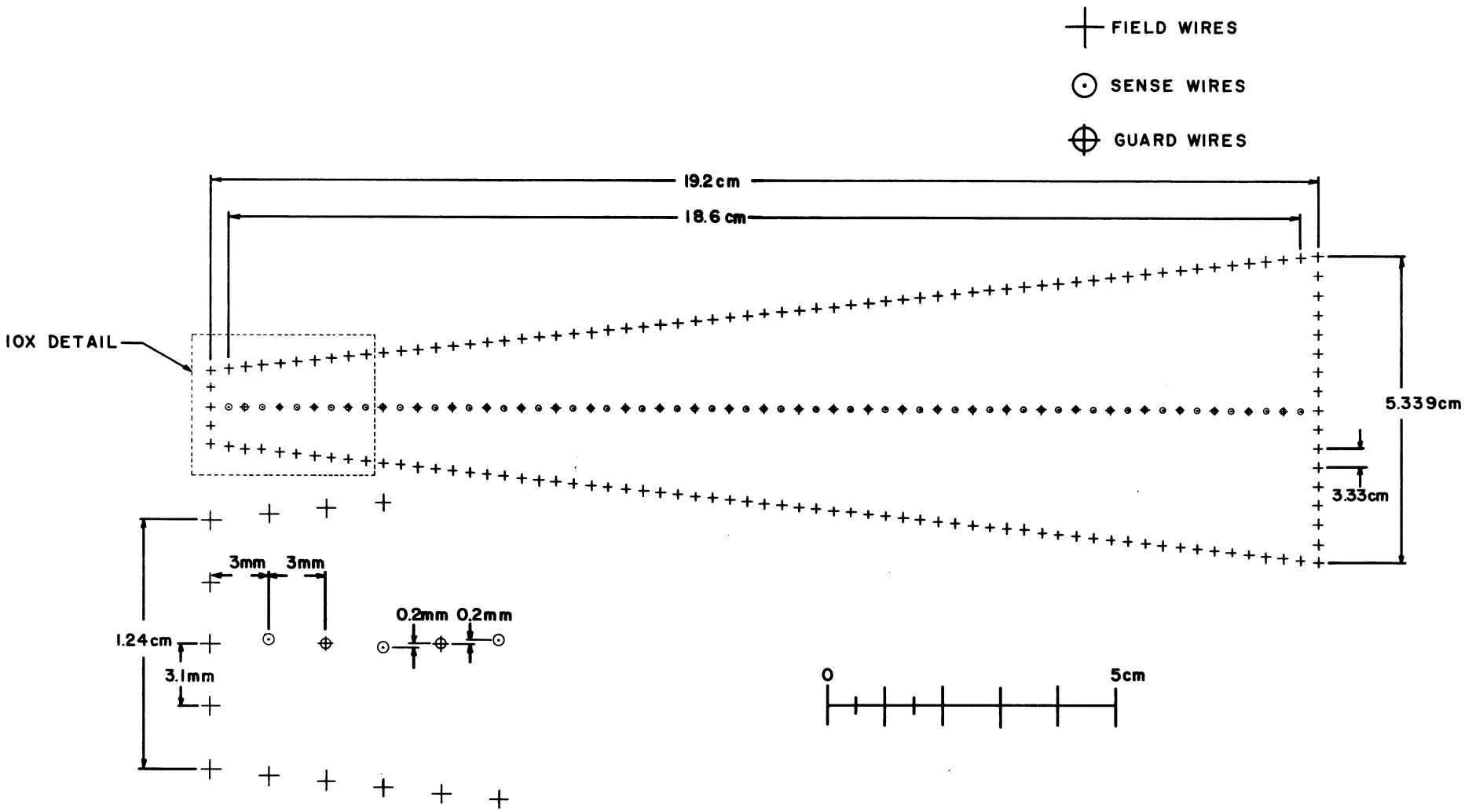

Fig. 25: One of the 30 JDC sectors.

A serious problem with using a drift chamber in a 1.5 T magnetic field is the distortion of the drift properties by the effect of the Lorentz force. We will use a "cool" gas in which the drifting electrons are thermalised by collisions with the molecules of the gas, and hence experience smaller Lorentz forces than in the more conventional "fast" gases[61]. CO2−Isobutane (90:10) mixtures have been studied by the SLD [62] and L3 [63] collaborations, and the Lorentz angle is expected to be 7^0 in a 1.5 T field.

Another advantage of a "cool" gas is the reduction in the longitudinal diffusion of the drift electrons[61]. This has made it possible to obtain spatial resolutions of 40 μm (L3) and 60 μm (SLD) for a 1 cm drift distance in tests of prototype chambers. For a chamber operating at a pressure of 1 atm with a maximum drift distance of 2.7 cm we assume that we can obtain a resolution of 100 μm. The precision with which sense wires can be positioned is expected to be 30 μm.

A disadvantage of a "cool" gas is that the drift velocity is not saturated, but depends linearly upon the electric field[63]. We have simulated the drift characteristics of our cell design, and obtained the drift velocity shown in Fig. 26. Careful parametrisation of the time−distance relationship is necessary to obtain good resolution. It will be necessary to control gas pressure and high voltages to <0.1 %, and temperature to $< 1^0$ [62].

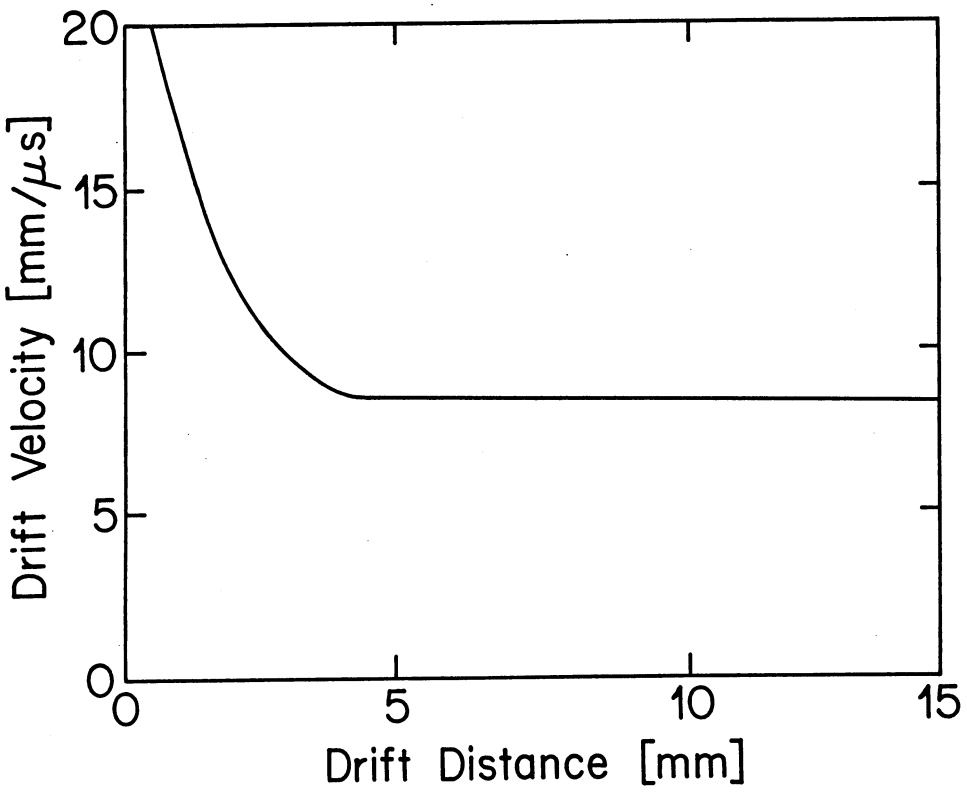

Fig. 26: Drift velocity vs distance from the wires.

Preamplifiers will be placed directly on the endplates of the chamber. We intend to use a miniaturised version of a hybrid circuit designed by V.Radeka (BNL). This preamplifier is being used for the vertex TPC of the CDF detector[64]. It has a rise time of 6 ns and a decay time of 30 ns, with a gain of 235 mV/pC for an input equivalent noise of $\simeq$ 4000 electrons. A charge division resolution of 0.7 % of a wire length has been obtained in prototype tests at Fermilab using a gain of 5×10^4.

The output signals from the preamplifiers are carried by miniature 56 Ω coaxial cables to the digitising electronics outside the magnet. We anticipate using a Flash ADC system to digitise the drift chamber information. An Flash ADC system is preferable to a single ADC/TDC system for three reasons:

1. Measuring the pulse shape can improve upon leading edge timing at large drift distances[63].

2. The ability to measure several tracks in one sector is useful because of the high event rates in the detector (up to 10^5 events/s).

3. The detailed record of the ionisation fluctuations is useful for refining the dE/dx measurements.

Several Flash ADC systems are now available, including those designed for UA1, OPAL and L3. As an example of the state of the art, the L3 system has a 100 MHz sampling rate and uses one microprocessor per channel to digitize all drift information in 1 ms.

A program of prototyping the JDC has begun at two of the participating institutions. Various cells are being built, including one with the design parameters specified in Table 12, but also cells with different wire spacings, wire materials, mechanical construction techniques and gases. The final parameters chosen for the JDC will be based on the resolutions achieved, susceptibility to breakdown, aging properties and mechanical integrity of the prototypes. In view of the limited access to the JDC we require a chamber that can be operated reliably over a period of several years.

5.6 CsI Barrel

We have chosen CsI(Tl) as the scintillation material[65]. The presence of a strong (1.5 T) magnetic field requires the use of photodiodes for the readout of the scintillation light. The light output of CsI is equivalent to that of NaI. The CsI emission spectrum is most prominent at the longer wavelengths and thus better matched to the response of photodiodes than to S11 photomultiplier cathodes. Also the hygroscopic nature of NaI(Tl) requires bulky vacuum tight vessels. This results in a smaller effective solid angle and no flexibility for changes in geometry. Finally, the price of CsI(Tl) is not very much higher than that of NaI(Tl) taking into account the difference in radiation lengths. Table 13 shows a comparison of CsI with NaI.

Parameter	CsI	NaI
Density [g/cm^3]	4.53	3.67
Radiation length [cm]	1.86	2.59
Hadronic absorption length [cm]	36.4	41.3
Average wavelength [nm]	550	410
Decay constant [ns]	900	230
Photon yield/MeV	4.5×10^4	4.0×10^4
Hygroscopy	no	yes
Mechanical stability	very good	fair (cleavage)
Price for large quantities [SFr/cm^3]	4.6	2.5

Table 13: Comparison of CsI(Tl) with NaI(Tl).

The shower containment and hence the energy and angular resolutions depend on the crystal size. We have studied the longitudinal and transverse shower developments with the Electron Gamma Shower program, (EGS4 [52]). The effect of a 1.5 T magnetic field was included.

Fig. 27 shows the energy deposition as a function of crystal length (up to 19 radiation lengths, X_0) for photons of various incident energies. Only 0.6 % of the energy is contained in the last 3 X_0 for 100 MeV (2.0 % for 2 GeV). There is a considerable improvement in energy resolution from 14 to 16 X_0 (Fig. 28). On the other hand, the gain in resolution for $L > 16\ X_0$ is not very significant and might be partially suppressed by a worse signal to noise ratio for a longer module.

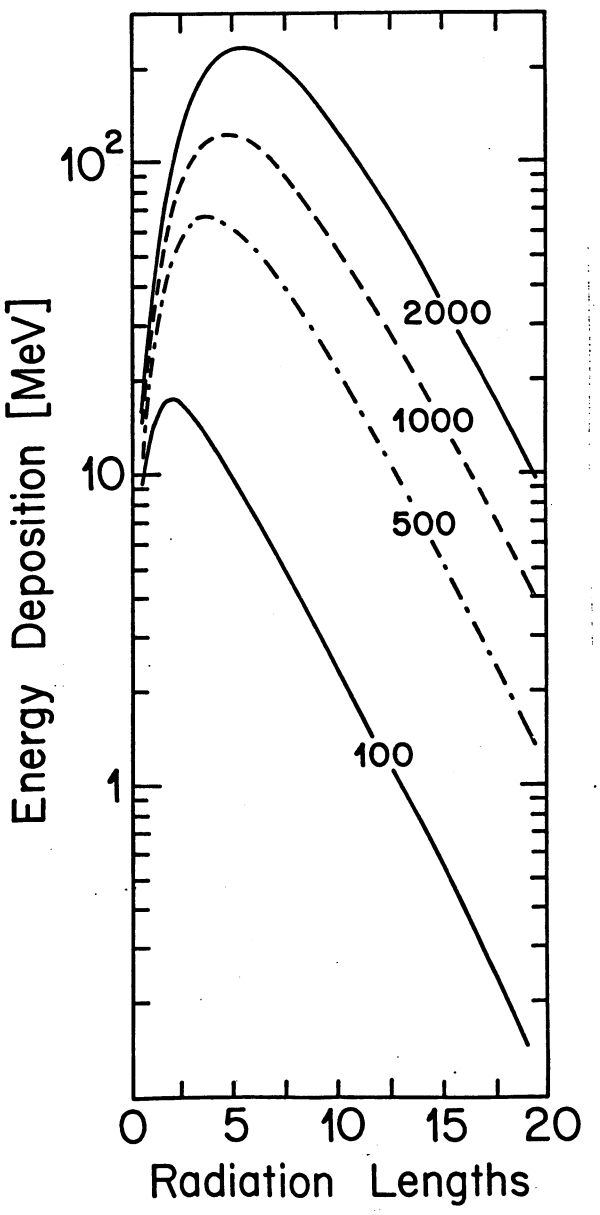

Fig. 27: Energy deposition in the longitudinal direction for incident γ energies of 100 MeV, 500 MeV, 1000 MeV and 2000 MeV.

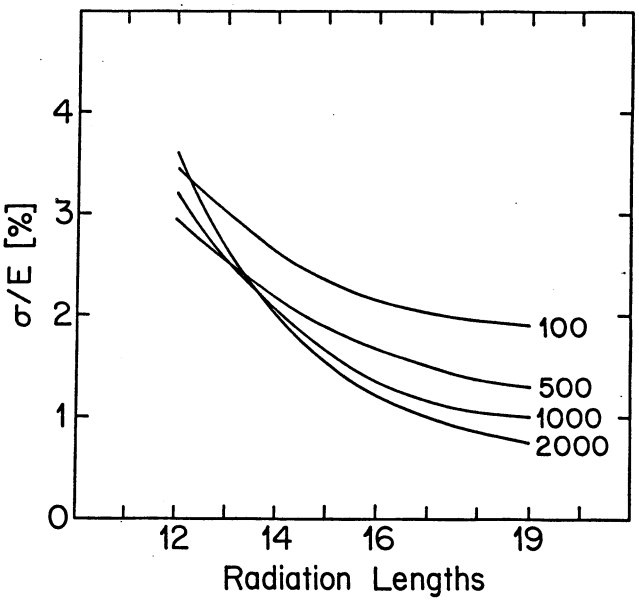

Fig. 28: Energy resolution as a function of crystal length for incident γ energies 100 MeV, 500 MeV, 1000 MeV and 2000 MeV.

The transverse extension of the shower produced by a photon hitting a CsI crystal (Fig. 29) requires a small cross section for the modules ($1-2\,cm^2$) to achieve good angular resolution. However, this would lead not only to a substantial increase in price, but also to a deterioration of the energy resolution, since the signal to noise ratio would be worse and the outputs of many more modules would have to be summed. Monte Carlo studies show that a tapered module of 3 by 3 cm^2 at the entrance leads to an angular resolution σ of about 20 mrad at 200 MeV (see Fig. 9).

We therefore decided upon a 30 cm (16 X_0) long tapered module, 3 by 3 cm^2 typically at the inner radius, to optimize the energy and angular resolutions and to minimize the cost. Each crystal covers 6^0 in θ and 6^0 in ϕ (12^0 in ϕ in the forward and backward directions). This leads to 13 different crystal shapes. The sizes are given in Fig. 30 and Table 14.

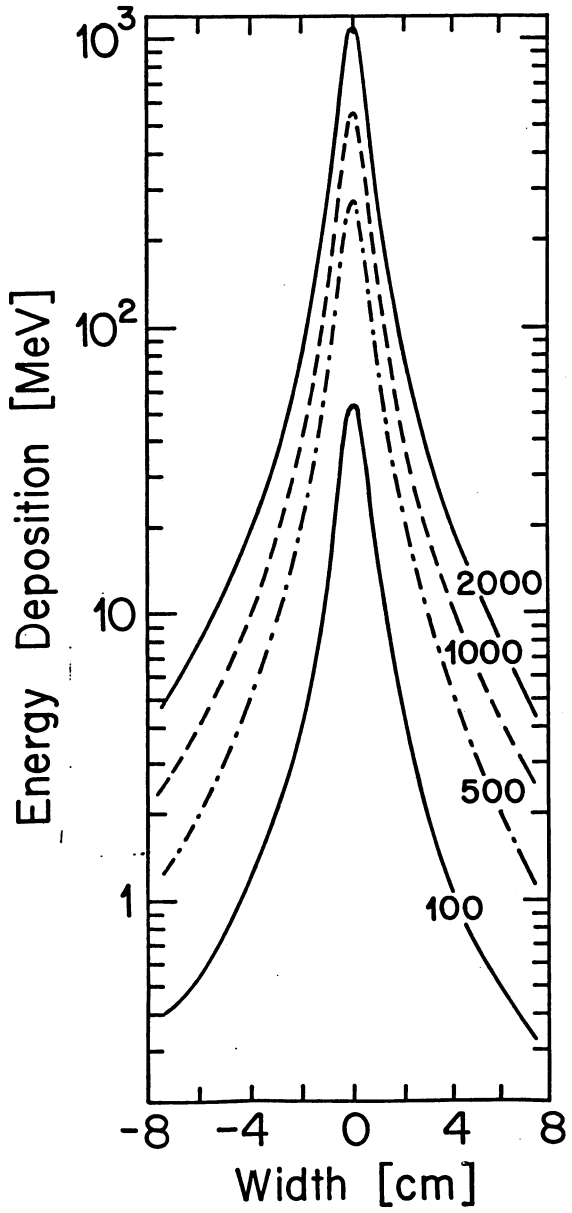

Fig. 29: Energy deposition in the transverse direction for incident γ energies of 100 MeV, 500 MeV, 1000 MeV and 2000 MeV.

No.	a[cm]	b[cm]	d[cm]	a'[cm]	b'[cm]	d'[cm]	#	[cm³]
1	2.951	2.935	2.947	6.100	6.066	6.091	120	637
2	2.984	2.935	2.996	6.115	6.015	6.141	120	643
3	3.018	2.935	3.082	6.098	5.930	6.226	120	651
4	3.055	2.935	3.208	6.050	5.811	6.353	120	663
5	3.096	2.935	3.384	5.972	5.662	6.529	120	679
6	3.142	2.935	3.623	5.869	5.482	6.767	120	700
7	3.195	2.935	3.944	5.742	5.275	7.088	120	729
8	3.089	2.781	4.150	5.429	4.888	7.295	120	712
9	2.643	2.321	3.944	4.749	4.172	7.088	120	590
10	2.132	1.814	3.623	3.983	3.388	6.767	120	454
11	Special shape see Fig. 30						60	704
12	2.621	1.994	3.208	5.189	3.947	6.353	60	510
13	1.912	1.290	3.082	3.864	2.606	6.226	60	350

Table 14: Dimensions of Crystal Barrel modules.

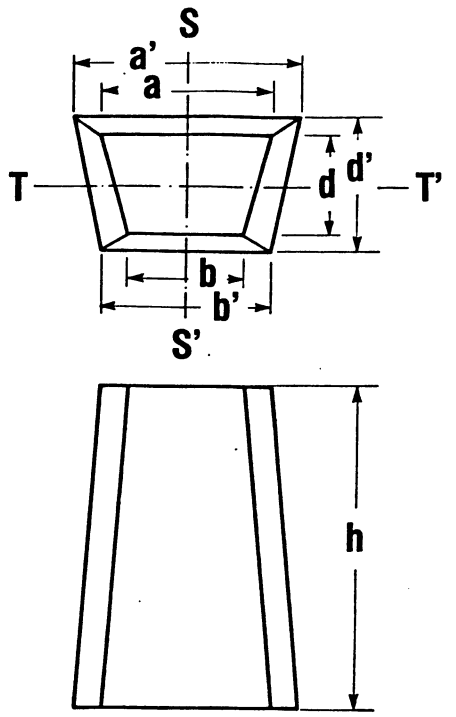

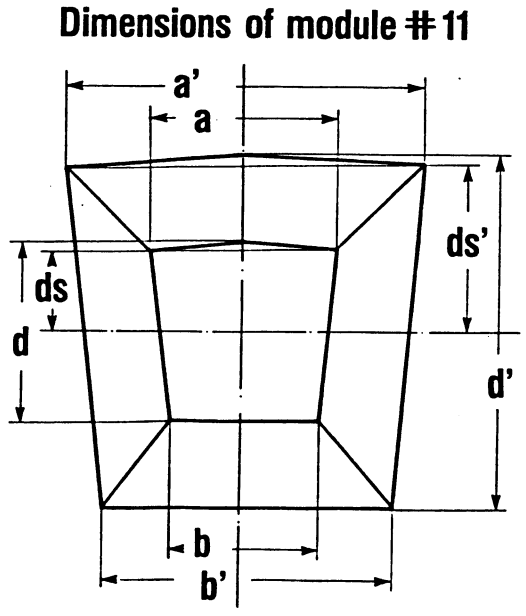

MODULE NO. 11

FRONTFACE
a = 3.407 cm
b = 2.769 cm
d = 3.385 cm
ds = 1.616 cm

REAR FACE
a' = 6.568 cm
b' = 5.341 cm
d' = 6.530 cm
ds' = 3.116 cm

Fig. 30: CsI crystal shapes

5.6.1 Energy Resolution

The most important parameters which determine the final energy resolution are: crystal length, transverse dimensions of the crystal cluster, materials in front and between crystals, longitudinal light collection uniformity, electronic noise and intercalibration between modules.

With 16 radiation lengths, energy leakage out of the rear of the crystal becomes significant only for $E\gamma > 1$ GeV (Fig. 27). The lateral energy leakage (Fig. 29) depends on the number of modules added to the central module. Fig. 31 shows the energy resolution (σ/E) calculated by EGS as a function of photon energy for the sum of 9 and the sum of 25 modules (electronic noise is folded in as explained later). One sees that for higher energies, the energy resolutions with 9 and 25 modules added become similar. This is fortunate, since it will allow better identification of high energy π^0's. At low energies ($E < 100$ MeV), the resolution is dominated by electronic noise.

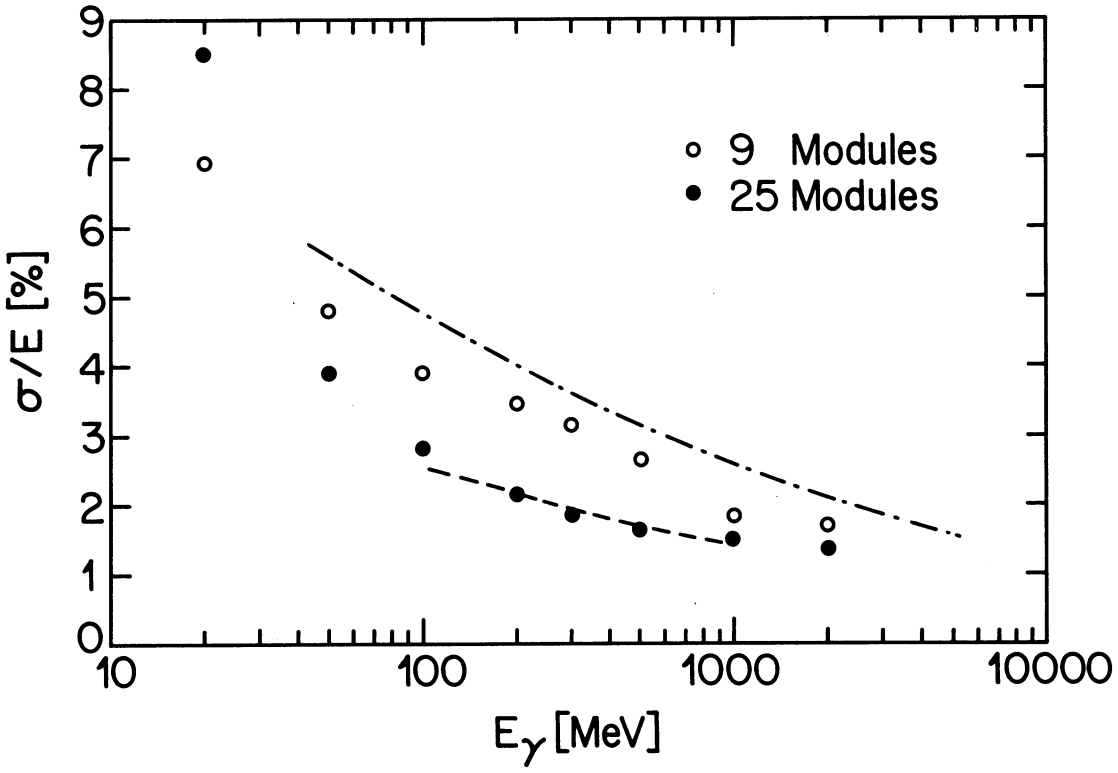

Fig. 31: Energy resolution of the Crystal Barrel as a function of γ energy. Results are from EGS simulation with 0.3 MeV RMS noise/module and 1.5 T magnetic field, for 25 modules added (full circles) and 9 modules added (open circles). Also shown are experimental results for the Stanford Crystal ball (dot – dashed curve) and the NaI Sector (ref [50], dashed curve).

Material between the target and the barrel, and between modules will be minimized. Its influence on the energy resolution will be small compared to that of other parameters. For example, 1 cm of aluminum (11% X_0) in front of the barrel changes the energy resolution at $E\gamma = 100$ MeV by less than 0.1%, and the situation improves with increasing energy.

Another important parameter is the uniformity of light collection along the crystal length. Simulation by the CLEO − II collaboration [51] shows that the deterioration of the energy resolution could be as high as 7 % for a 10 % non − uniformity in light output. We intend to impose on the manufacturers of the crystals a maximum non − uniformity of 5 % and as low as 2 % for the important first 10 cm, where 70 % (45 %) of the energy is deposited at $E\gamma = 100$ MeV (1 GeV). Thus, the influence of the non − uniformity will be negligible. This kind of uniformity specification has proven to be very successful in obtaining good energy resolution[50]. This is in fact the main reason for the better energy resolution achieved in the 54 module sector [50] compared to the Crystal Ball. Measurements on test modules have shown that these tight specifications can be achieved by the manufacturers, and they have accepted them.

The light output is measured by photodiodes. They have very good quantum efficiency (~80%) but no internal amplification, thus imposing the use of a low noise charge sensitive preamplifier. The photoelectron statistics (~3000 photoelectrons/MeV) is sufficient but the r.m.s. noise at the input of the preamplifier is around one thousand photoelectrons with shaping constants of some μs, thus influencing the resolution at low energy. Further sources of noise are the capacitance of the photodiode and the photodiode dark current. The last two parameters depend on the bias voltage, but their contributions to noise are of opposite sign. As a result, the noise is rather insensitive to the bias voltage, at least in the range 10 − 25 volts. Using four Hammamatsu S1723 − 04 (1 cm^2) photodiodes on a 5 by 5 by 30 cm^3 CsI(Tl) crystal and the MPI − Munich hybrid preamplifier[66], we obtain an r.m.s. noise equivalent of 0.3 MeV. This value for the noise was used in the calculated energy resolution shown in Fig. 31. The electronic noise, being independent of the energy, will contribute mostly at low energies (< 100 MeV) and will be negligible at high energies.

Another sensitive parameter is the readout threshold. A low threshold (e.g. $\approx$ 1 MeV) does not alter significantly the initial energy resolution but increases the number of modules to be read out. A good solution is to use a relatively high threshold (several MeV), but to read out systematically the 8 (or 24) modules surrounding a module with significant (~20 MeV) energy deposition.

Another way to further decrease the noise would be to use fluorescent flux concentrators[67]. It consists of a wavelength shifter adapted to the emission spectrum of CsI(Tl) centered around 550 nm and a small photodiode (< 1 cm^2). This type of light readout is at the present under investigation.

5.6.2 Absolute and Intercalibrations of the Modules

An important consideration in obtaining good energy resolution is an excellent energy calibration (to within 1 %) of all modules. Here one should distinguish between the initial absolute calibration of each module and the stability of this calibration during the experiment.

The first step is to obtain an absolute energy calibration at low energies. We intend to use the 6.14 MeV γ − ray emitted by a Pu − ^{13}C source. Fig. 32 shows the 6 MeV peak obtained in a 5 by 5 by 30 cm^3 CsI(Tl) test crystal read out by four photodiodes. The source was placed 28 cm from the entrance face of the crystal (corresponding to the distance from a crystal to the center of the barrel) and the neutron induced background was subtracted by inserting 2.5 cm of lead. This peak permits a calibration at the 1 % level in a few hours and gives a starting point for the next step.

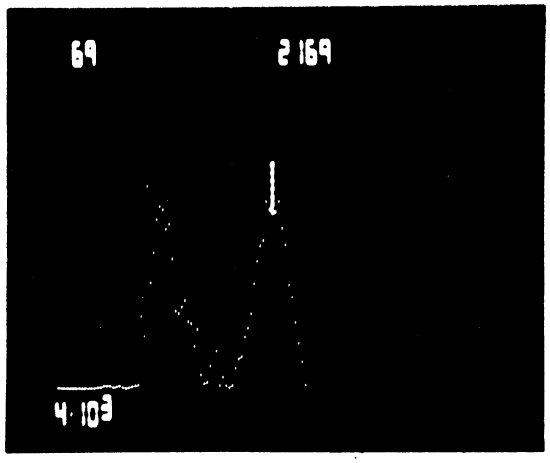

Fig. 32: Peak (at marker) produced by the 6.1 MeV γ − ray of a Pu − ^{13}C source in a 5 × 5 × 30 cm^3 CsI(Tl) crystal (after neutron background subtraction).

For the actual energy calibration we would expose each module (mounted in its final position in the barrel) to a photon (or electron) beam of a few hundred MeV. An iterative procedure gives the calibration factors of all modules to better than 1 % in the energy region of the experiment. The final calibration for 20−2000 MeV will be done with the 6 MeV source, the calibration points and EGS simulation of peak positions at other energies. The electronic linearity (including photodiodes) will be checked with a calibrated light pulser.

Another way to determine the calibration curve of an individual CsI module at higher γ energies is to use annihilation reactions. Of particular importance are the channels $(p\bar{p})\text{rest} \to \pi^0\gamma$ ($E\gamma = 933$ MeV), $\pi^+\pi^-\pi^0$ and $2\pi^+2\pi^-\pi^0$ The $\pi^0\gamma$ channel occurs with a branching ratio of 1.5×10^{-4} [68]. With a trigger on 3 γ's, after 4 hours of LEAR running with 10^5 $\bar{p}$/sec, about 150 events/module can be collected, giving rise to a good calibration at 933 MeV. For $\pi^+\pi-\pi^0$, $2\pi^+2\pi^-\pi^0$, the momenta of the charged pions measured in the JDC are used to reconstruct the π^0 momentum. The angles of the two γ's from the π^0 decay measured in the CsI detector determine uniquely the γ energies. Monte Carlo calculations show that for the $2\pi^+2\pi^-\pi^0$ reaction the γ energy can be determined with an error of about 1 % FWHM in the energy region of 50−500 MeV, while for the $\pi^+\pi^-\pi^0$, the error is typically twice as high (Fig. 33). The reactions occur with branching ratios of 20% ($2\pi^+2\pi^-\pi^0$) and 7% ($\pi^+\pi^-\pi^0$). Thus, with 4 hours of LEAR time and with a multi−prong trigger on these reactions, about 4000 γ's/module will be generated. The γ's are distributed over an energy range reaching 500 MeV ($2\pi^+2\pi^-\pi^0$) and 850 MeV ($\pi^+\pi^-\pi^0$).

The values of the calibration constants will be monitored during the experiment in two ways: (1) with a calibrated light pulser, the stability of which is monitored with a test crystal exposed to a radioactive source[50]; (2) with the minimum ionization peak of traversing pions (~170 MeV).

Also, the 6 MeV source could be inserted at any time.

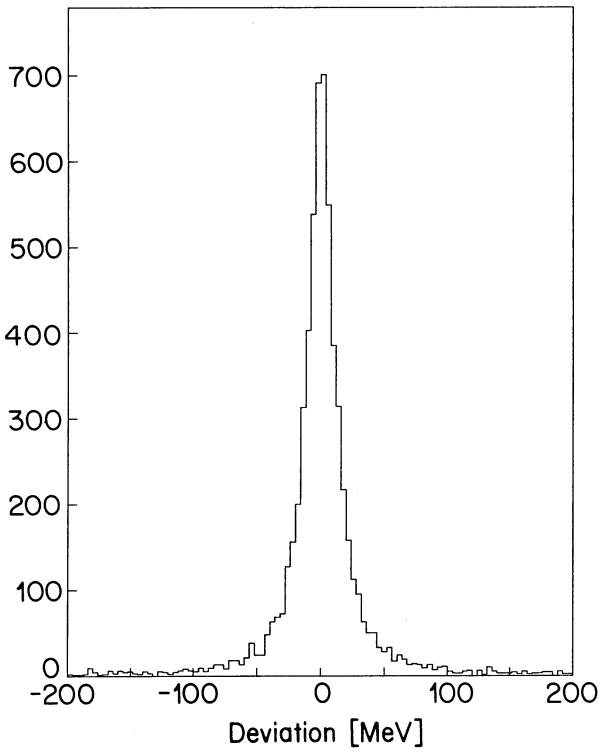

Fig. 33: Deviation of the measured γ energy from the calculated energy in $\pi^+\pi^-\pi^0$ (for γ energies around 300 MeV).

5.6.3 Crystal Durability

The mechanical ruggedness of the CsI makes it unlikely that a crystal requires replacement. The barrel should be kept in a dry atmosphere at a temperature between 22 and 25°C where the CsI(Tl) – photodiode assembly has been shown to be stable[51] and have pulse heights which are essentially temperature independent. Radiation damage to the crystals will be negligible in the Crystal Barrel environment: 1000 hours of operation at a rate of 10^5 $\bar{p}$/s would give a mean crystal dose of $\simeq$ 2 rad. A study of CsI radiation damage demonstrates changes in crystal light output and in light transmission only for doses of 100 rad [51].

5.6.4 CsI Tests

At present, 5 by 5 by 30 cm^3 CsI(Tl) crystals from three manufacturers (BDH, Bicron and Horiba) have been used for measurements with photodiodes and for light output uniformity checks. The results are very similar to those obtained by the CLEO – II collaboration[51]. Tests with a fluorescent flux concentrator[67] are underway.

A certain number (27) of CsI(Tl) crystals of different shapes corresponding to the Crystal Barrel modules have been ordered from the three manufacturers to test their capability to produce modules of the final shape according to our light output specification. We will construct a test detector of 25 modules for checking energy and angular resolutions, readout electronics, data acquisition and energy calibration procedures. This test detector will be ready at the end of 1985. The test with an electron beam will be performed at SIN.

5.6.5 Readout Electronics

Fig. 34 shows schematically the electronics associated with the 1380 CsI crystals of the barrel. Each crystal (1) receives light flashes from a light pulser via an optical fiber (2). The scintillation light intensity from the crystal is measured using photodiodes (3). A low noise charge sensitive preamplifier (4) converts the photoelectrons into a pulse which is put into a suitable form by a shaping amplifier (5). The shaping time is determined on the low side by the 0.9 μs scintillation decay time of the crystal and on the high side by pulse pile up. The shaping time will be typically 3 μs. The two amplifiers (hybrids) are located directly behind the crystal to minimize noise pick – up. A twisted – pair cable brings the output pulse to the discriminator (6), feeding the cluster trigger, and the ADC's (7). In order to cover the wide dynamic range (< 1 MeV to 2 GeV), two 11 – bit ADC's per module are foreseen: one (low range) covering 0 – 200 MeV, the other (high range) covering 0 – 2 GeV. For triggering purposes, we plan to use ADC's with fast conversion time (like LRS FERA's). The amplifiers will be designed in such a way that a future extension of the high range up to $\approx$5 GeV is possible by changing the attenuator (8).

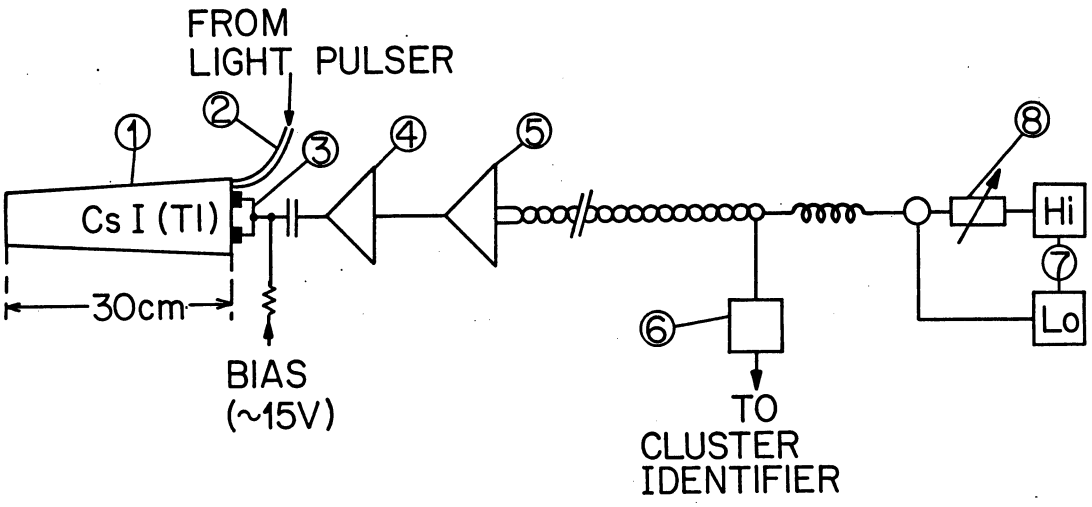

Fig. 34: Electronics for CsI modules (1380 channels).

5.7 Mechanical Assembly

The Crystal Barrel is divided into upper and lower halves forming a compartmental structure (Fig. 35). Each compartment holds 16 to 20 crystals. The crystals are wrapped first in teflon, then in aluminized mylar. The separation between compartments is provided by thin aluminium walls. The crystals are held in position from the back. The total assembly weighs 4 tons.

The complete detector is mounted on rails and can be rolled out of the magnet downstream on a moveable support for servicing (Fig. 36). The upper (lower) half can be raised (lowered) to give access to the central detector. The barrel can be rotated around its horizontal axis for loading the crystals and for calibration in an electron beam.

Signal and high voltage cables from the JDC and PWC/XDC will leave the downstream end of the detector through the forward tunnel of the barrel. Signal cables from the upstream preamplifiers (1 % radiation length) will pass between the JDC outer shell and the barrel.

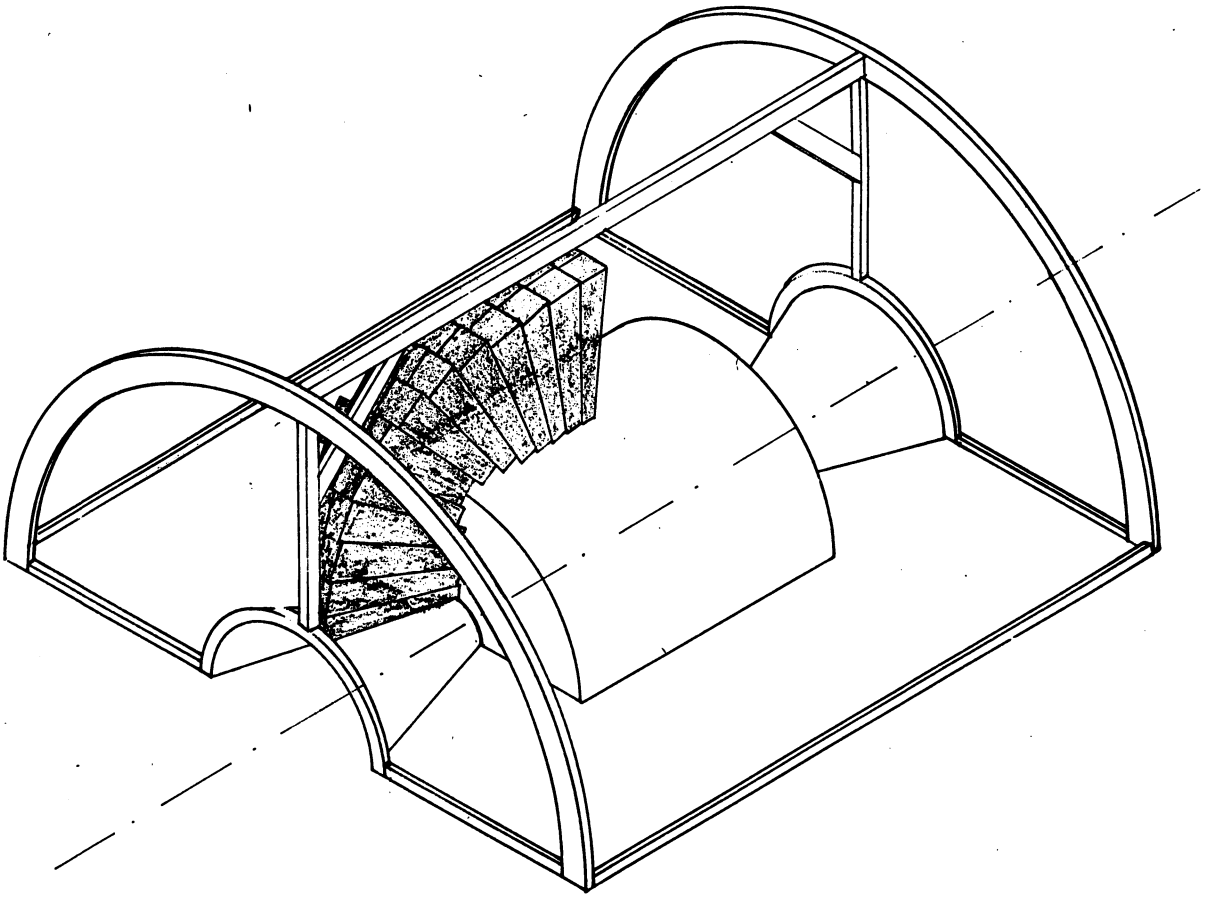

Fig. 35: Upper half of the barrel support frame.

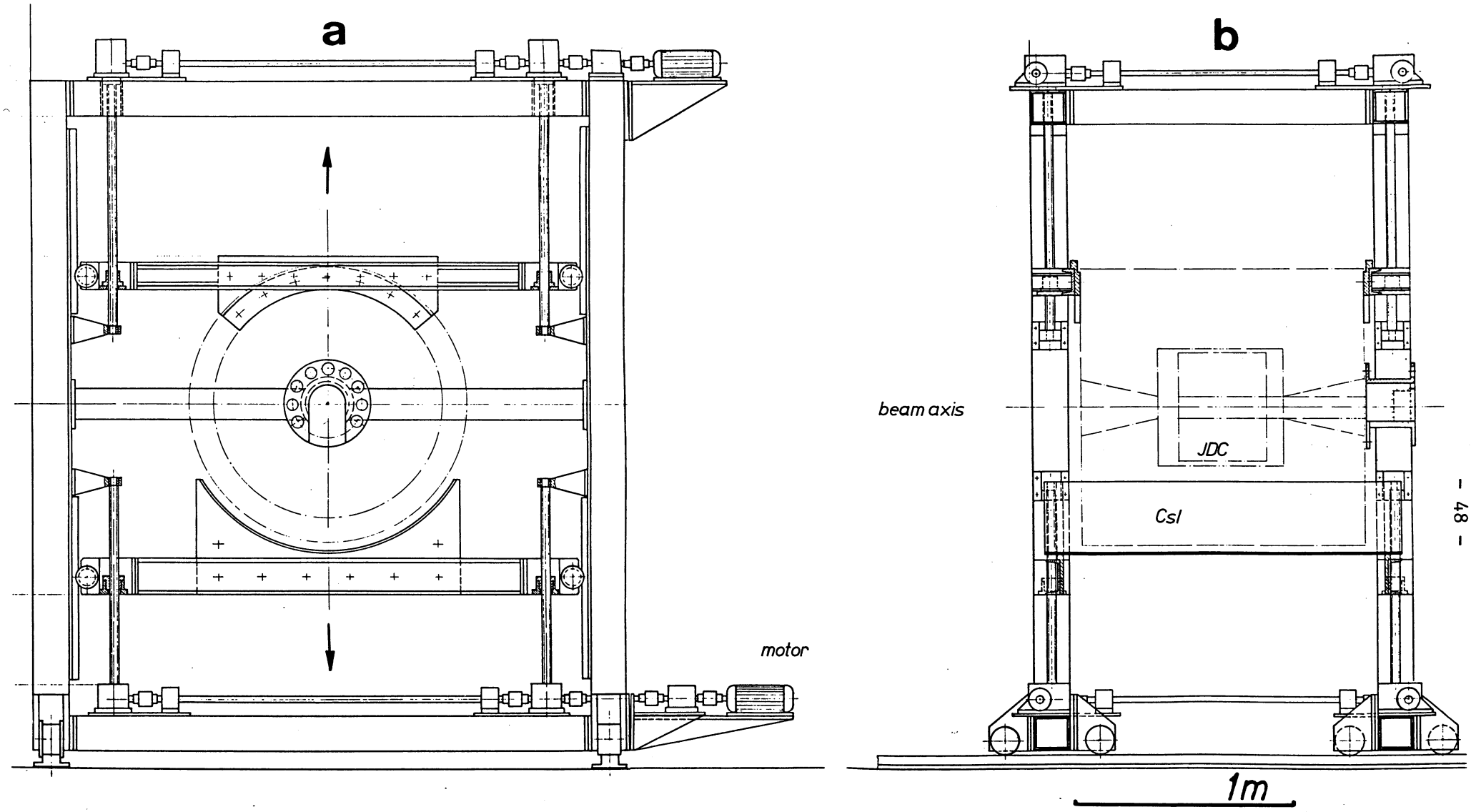

Fig. 36: Maintenance carriage for the Crystal Barrel.
(a) front view, (b) side view.

5.8 Trigger Electronics and Data Acquisition

We will take data in two principal modes:

1. An unbiased mode in which all annihilation events are written to tape, limited in rate by the data writing capability of the system.

2. A triggered mode in which specific channels will be investigated, limited in rate by the system dead time.

Fig. 37 shows a schematic overview of the electronics system. The decision times in the third column are based on one of the channels simulated above, namely $\bar{p}p \rightarrow \pi^{\pm}X^{\mp}$, where X is a hybrid decaying finally into $\pi^{\mp}\pi^0\pi^0\eta$. The system selects in this example events with two charged particles and 6 γ's with invariant masses consistent with two π^0's and one η. In the following we briefly describe the five different levels of the trigger system.

Trigger level 0 defines an incoming $\bar{p}$.

Trigger level 1 is, from the point of view of event reduction, the most important level. With a decision time of 3 μs, essentially determined by the pulse shape of the CsI amplifier outputs, this level is able to handle a rate of 3 x 10^5 events/s. The multiplicity of charged tracks in the PWC or XDC is derived by a cluster logic, as currently used in most wire chamber systems. To get the total multiplicity (the number of clusters in the barrel) a "projection" trigger will be used: by taking an OR of the discriminator outputs of all crystals with the same z coordinate, one gets a projection of hit clusters in the z direction. The multiplicity in this projection is determined by the same type of majority logic as for the PWC. To be able to separate two clusters with the same z coordinate one also forms the projection in the ϕ and in the diagonal directions. Finally, the difference between total and charged multiplicity (derived from the XDC or PWC) yields the neutral multiplicity.

Several multiplicity patterns or ranges will be permitted simultaneously. If the event is discarded, the digitizing of the JDC and the crystals are reset.

For each CsI crystal a CAMAC readable bit is set during the decaytime of the signal ($\simeq$ 100 μs) to flag pile up events. At the output of this trigger level we will get in our example 6 x 10^3 events/s mostly coming from the channel $\pi^+\pi^-3\pi^0$. This rate can be handled by the next stage with 50 % deadtime.

Trigger level 2 consists essentially of a CAMAC based microprocessor (CAB) with a cycle time of 200 ns. Since the FERA ADC's are able to perform an automatic pedestal subtraction and to suppress the readout of empty channels, the CAB gathers the hit information through fast ECL bus (10 MHz) in 20 μs (assuming eight clusters with nine crystals each). Sorting the hits into clusters and multiplying by a calibration constant takes 150 μs. A more precise decision on total multiplicity can be done at this point, as well as imposing constraints for the minimum and maximum energy per cluster.

If the event is accepted, the cluster information is sent over CAMAC to level 4, a starburst microprocessor (based on a 11/73 VLSI), equipped with a floating point booster. Here all possible combinations of 2γ invariant masses are computed until a suitable $\pi^0\pi^0\eta$ final state is found. The average processing time is 250 μs. With this requirement about 20 events/s survive in our example. If the event is accepted, the JDC and FERA information is read from CAMAC. Several events are packed together in large data blocks which are then sent to a VAX 750 over an usual system crate interface. The data is then saved on tape and an online sampling analysis is performed.

To measure the acceptance of the trigger system, Monte Carlo generated events can be fed into trigger level 1. In addition the system handles the light diode calibration procedure.

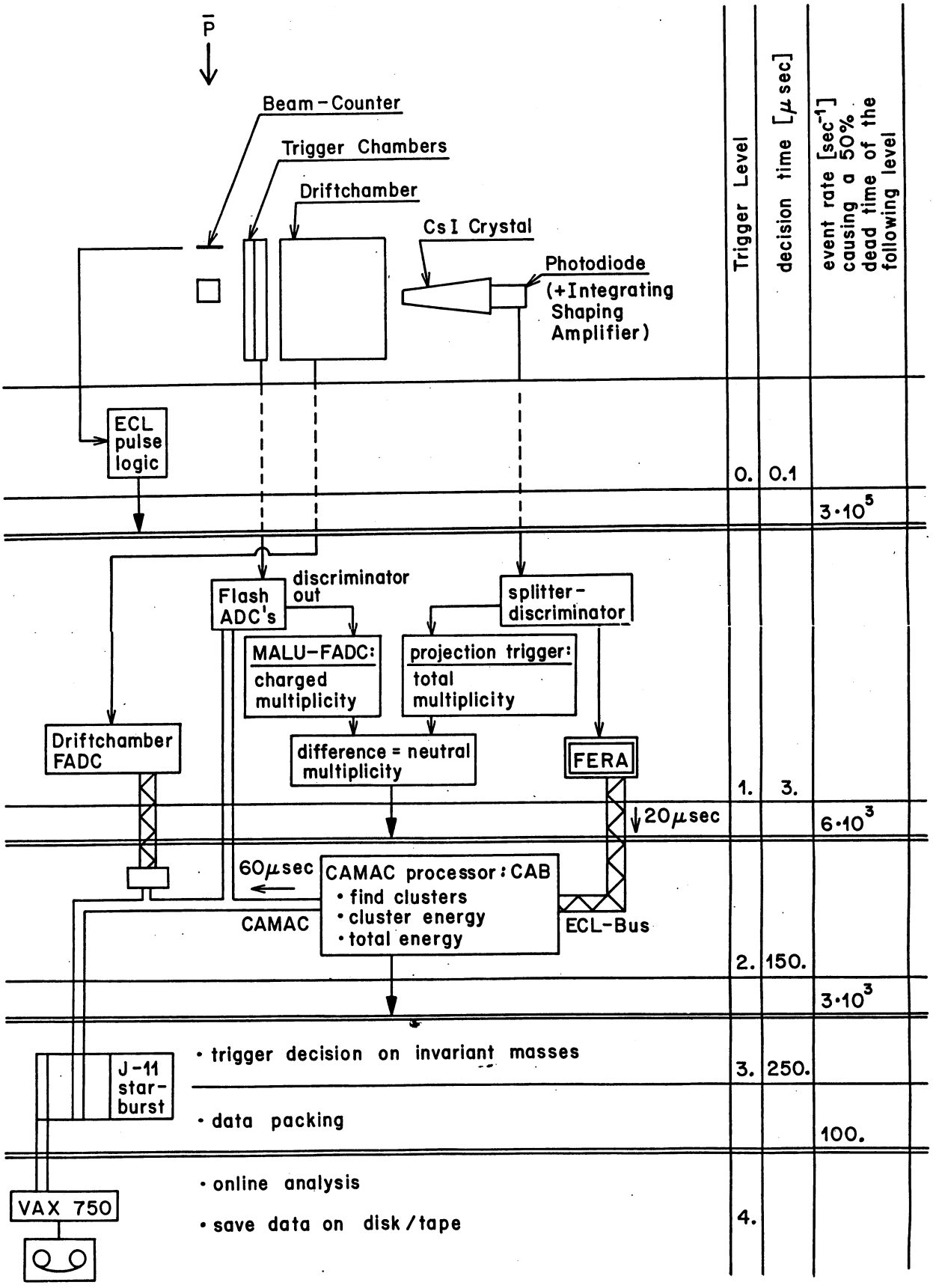

Fig. 37: Flow diagram for the fast trigger (see text).

6. COSTS AND RESOURCES

All participating institutions already work at LEAR (PS171, 172, 176, 183) and have considerable equipment which will be available for the Crystal Barrel experiment. This includes PWC and XDC chamber readout electronics, fast electronics, racks, crates, cables, etc. Also, the infrastructure of PS171 will be available. The additional costs are (in MSFr):

CsI barrel:	Crystals (869 litres)	4.0
	Electronics: (photodiodes preamplifiers, shaping amplifiers)	0.4
	ADC's(2760 channels)	1.0
	Mechanics	0.3
PWC/XDC/JDC:	Mechanics	0.3
	JDC electronics	0.7
Magnet:	New coil, additional shielding	0.3
Trigger:	Maj. logic, CAB, J−11	0.3
	TOTAL	7.3

The total funds required are balanced by the contributions of the collaborating institutions (subject to approval by the different funding agencies). The contributions for the three years 1986 − 1988 would be divided as follows (MSFr):

Irvine	0.75
KfK Karlsruhe	2.60
Uni Karlsruhe	0.80
Queen Mary	0.20
Mainz	0.80
München	0.80
Penn State	0.75
Surrey	0.20
Wien	0.10
Zürich	0.30
Total	7.30

Parts of the collaboration have already experience in operating a large modular γ detection system (PS161) and in constructing and operating large chambers and triggers (PS171, 172, 183). Support from the home machine and electronics workshops will be available.

7. REQUESTS TO CERN

The proposed experimental program requires an extracted $\bar{p}$ beam from LEAR with a momentum range 0.1 − 2.0 GeV/c. The transverse beam size at the beam counter should be less than or equal to σ = 3 mm and the momentum bite $\simeq 3 \times 10^{-3}$ or less. The intensity of the beam should be $\simeq 10^5$ $\bar{p}$/s at 0.1 − 0.2 GeV/c and $\simeq 10^6$ $\bar{p}$/s at 2 GeV/c.

The floor space required for the experiment is equivalent to that now occupied by PS171 (ASTERIX), an area approximately 11 m along the beam direction and 7 m transverse to the beam direction. The counting house now used is suitable (dimensions 12 m by 4 m).

The modification of the present DM1 magnet will be the responsability of the collaboration. We request that CERN install the magnet (power and water) and assist us with the mapping of the magnetic field.

The gas target will be an integral part of the XDC and will be provided by the collaboration. We request that CERN design and construct the LH_2 target.

We request that CERN provide the gas systems for the wire chambers.

Most of the data analyses will be done at the collaborating institutions, where the equivalent of 2000 IBM 3081 CPU hours are available per year. However since most of the physicists will be resident at CERN during the running periods, we request 400 IBM CPU hours per year on the central computer for monitoring of data quality and preliminary analyses. We also need a link from the experiment to the IBM.

We also request access to the CERN Electronics Pool to the same extent as is presently the case for the groups working at LEAR (PS 171, 172, 176, 183).

We anticipate that the Crystal Barrel will be completed by early 1988.

7.1 Beam Time Request

We require approximately 3 weeks of low intensity parasitic beam at low momentum in order to setup and calibrate the apparatus. This will be performed with the liquid hydrogen target.

We request 200 spills of beam time for the work at rest with liquid at 10^5 $\bar{p}$/s. We anticipate devoting a fraction of the allocated time to non selective data taking. We will then implement selective triggers to obtain large samples on particularly interesting topics like:

1. Search for glueballs and exotics in decay modes like $\pi^0\pi^0$, $\pi^0\eta$, $\eta\eta$, $\pi^0\pi^0\eta$ and $\pi^+\pi^-\eta$. In particular we will study the E/ι decay modes, e.g. E → $\pi^0\pi^0\eta$, $\pi^+\pi^-\eta$, $K\bar{K}\pi$ and $\rho\gamma$ in $\bar{p}p$ → $E\pi^+\pi^-$.

2. Study of the annihilation mechanism ($\bar{p}p$ → $\pi^0\pi^0$, $\pi^0\eta$, $\eta\eta$, $\pi^0\eta'$ and $\eta\eta'$).

3. Meson spectroscopy, for example search for H′ → $\eta\omega$ in $\bar{p}p$ → $\pi^0\eta\omega$ and A_2 → $\eta'\pi$ in $\bar{p}p$ → $A_2\pi$ and search for D′ → $K_S K\pi$ in $\bar{p}p$ → π^0D′.

We request 100 spills for annihilation at rest in gas with the trigger on atomic L X−rays.

We need 200 spills at 2 GeV/c at an intensity of $\simeq 10^6$ $\bar{p}$/s to search for

1. hybrids e.g. $\bar{p}p$ → πX (X → πD, D → $\eta\pi\pi$) or (X → πB, B → $\omega\pi$) .

2. high mass glueballs (1600 to 2200 MeV) in reactions like $\bar{p}p$ → $\pi^0\Theta$ (Θ → $\pi^0\pi^0$, $\eta\eta$, $\eta\eta'$).

Eventually we would like to use the scanning mode of LEAR to do systematic studies of branching fractions and partial waves in exclusive channels. For these measurements, we would need to step in small intervals between 200 MeV/c and 2 GeV/c, taking an appropriate number of spills at each momentum. A specific request will be made later.

8. REFERENCES

1. P.M. Fishbane and S. Meshkov, Comments on Nucl. Part. Phys. 13 (1984) 325.
   F.E. Close, Nucl. Phys. A416 (1984) 55.
   G.A. Smith, SIN Spring School on Strong Interactions, Zuoz (1985).
2. K. Ishikawa et al., Phys. Letters 120B (1983) 387.
3. V.A. Novikov et al., NP B191 (1981) 301.
   S. Narison, Z. Phys. C26 (1984) 209.
4. T. Barnes, Z. Phys. C10 (1981) 275.
   J.M. Cornwall and A. Soni, Phys. Letters 120B (1983) 431.
5. N. Isgur and J. Paton, Phys. Rev. Letters D31 (1985) 2910.
6. R. L. Jaffe and K. Johnson, Phys. Lett. 60B (1976) 201.
7. J. F. Donoghue, International Europhysics Conference on High Energy Physics, Bari(1985).
8. D. V. Bugg, submitted to Phys. Letters.
9. M. Chanowitz, Phys. Rev. Lett. 46 (1981) 981.
10. A. Billoire et al., Phys. Lett. 80B (1979) 381.
11. R. Lacaze and H. Navelet, Nucl. Phys. B186 (1981) 247.
12. J. L. Rosner, Phys. Rev. D24 (1981) 1347.
13. C. Daum et al., Z. Phys. C23 (1984) 339.
14. V. Chabaud et al., Nucl. Phys. B223 (1983) 1.
15. A. Etkin et al., Phys. Rev. D25 (1982) 1786.
16. M. Chanowitz and S. Sharpe, LBL preprint LBL−16489 (1983).
17. H. Goldberg, Phys. Rev. Lett. 44 (1980) 363.
18. V. Novikov, M. Shifman, A. Vainshtein and V. Zakharov, Phys. Lett. 86B (1979) 347.
19. N. Isgur, R. Kokoski and J. Paton, Phys. Rev. Lett. 54 (1985) 869.
20. C. Amsler, Proc. of the Third LEAR Workshop, Tignes (1985).
21. B. Diekmann, Habilitationsschrift, Universität Bonn, 1984.
    L. Montanet, Rep. Prog. Phys. 46 (1983) 337.
    L. Montanet, Proc. Exp. Meson Spectroscopy Conf., Brookhaven, (1983).
22. R. Armenteros et al., Proceedings of the Sienna Conference on Elementary Particles 1 (1963) 287.
23. P. Gavillet et al., Z. Phys. C16 (1982) 119.
24. P.J. O'Donnell, Rev. Modern Phys. 53 (1981) 673.
25. A.M. Green and J.A. Niskanen, Nucl. Phys. A430 (1984) 605.
26. A. Faessler, Progr. Part. and Nuclear Phys. 11 (1983) 171.
27. M. Kohno and W. Weise, Phys. Letters 152B (1985) 303.
28. C.B. Dover and P. Fishbane, Nucl. Phys. B244 (1984) 349.
    C.B. Dover, Int. Symp. on Medium Energy N and $\bar{N}$ Scattering, Bad Honnef, 1985, BNL preprint 36821.
29. H. Genz, Phys. Rev D28 (1983) 1094, D31(1985) 1136.
30. U. Hartmann, E. Klempt and J.G. Körner, Phys. Letters 155B (1985) 163.
31. M. Poppe, Hadron Spectroscopy Conference, College Park, USA (1985).
32. R.S. Dulude et al., Phys. Letters 79B (1978) 329.
33. T. B. Day, G.A. Snow and J. Sucher, Phys. Rev. 118 (1960) 864.
34. C. Ghesquière, Symp. on Antinucleon Nucleon Interactions, Liblice, Yellow Report CERN 74−18 (1974) 436.
35. M. Foster et al., Nucl. Phys. B6 (1968) 107.
36. S. Devons et al., Phys. Letters 47B (1973) 271.
37. R. Bizzarri, Symp. on $N\bar{N}$ annihilation, Chexbres, (1972) 161.
38. S. Ahmad et al., Proc. of the Third LEAR Workshop, Tignes (1985).

39. S. Devons et al., Phys. Rev. Letters 27 (1971) 1614.
G. Bassompierre et al., Proc. 4th European Antiproton Symp., Barr, Vol I (1978) 139.
40. S. Ahmad et al., Phys. Letters 157B (1985) 333.
41. S. Ahmad et al., Proc of the 7th European Symposium on Antiproton Interactions, Durham, (1984) 131.
42. P. Gavillet, Thèse 3ème cycle, Grenoble, (1968).
43. For a recent review see C. Amsler, Habilitationsschrift, Universität Zürich, 1985.
44. B. Richter et al., Phys. Letters 126B (1983) 284.
45. UC Irvine, Penn State Univ., see M. Mandelkern, Proc. of the Third LEAR Workshop, Tignes (1985).
46. C. Defoix et al., Nucl. Phys. B162 (1980) 12.
47. K. Nakamura and T. Tanimori, Proc. VII European Symp. on Antiproton Interactions, Durham, (1984).
48. S. Ahmad et al., Phys. Letters 152B (1985) 135.
49. See for example J.E. Gaiser, Thesis, SLAC report 255, (1982).
50. P. Blüm et al., Nucl. Instr. Methods 213 (1983) 251.
51. CLEO II proposal, Report CLNS 85/634, (1985).
52. W.R. Nelson et al., EGS4 User Manual.
53. C.D. Edwards, Thesis, Caltech report CALT 68−1165, (1985).
54. R. Armenteros et al., CERN proposal PS171, 1980.
55. V. Flaminio et al., Compilation of p and $\bar{p}$ cross sections CERN−HERA 84−01.
56. P. Baillon et al., Il Nuovo Cimento 50A (1967) 393.
57. J.P. Stroot, CERN EP 85−01, 1985.
58. S.M. Ganguli et al., Nucl. Phys. B183 (1981) 295.
59. Z. Ming Ma et al., Nucl. Phys. B51 (1973) 77.
60. H. Drumm et al., Nucl. Instr. Methods 176 (1980), 333.
61. J. Va'vra, CERN preprint EF/84−17 (submitted to Nucl. Instr. Methods).
62. SLD design report.
63. V. Commichau et al., Nucl. Instr. Methods A235 (1985) 267.
64. R. Yarema, Fermilab report CDF TM−1284.
65. M. Suffert, Proc. of the Third LEAR Workshop, Tignes, (1985).
66. Kindly supplied by E. Lorenz, MPI Munich.
67. E. Lorenz, private communication.
68. G. Backenstoss et al., Nucl. Phys. B228 (1983) 424.